Research Paper
Computational Methods for Differential Equations
http://cmde.tabrizu.ac.ir
Vol. 11, No. 4, 2023, pp. 753-775
DOI:10.22034/cmde.2023.51339.2136

Infinitely smooth multiquadric RBFs combined high-resolution compact discretization for nonlinear 2D elliptic PDEs on a scattered grid network

Navnit Jha* **and Shikha Verma**

Department of Mathematics, South Asian University, Maidan Garhi, New Delhi-110068, India.

Abstract

Multiquadric radial basis functions combined with compact discretization to estimate solutions of two dimensions nonlinear elliptic type partial differential equations are presented. The scattered grid network with continuously varying step sizes helps tune the solution accuracies depending upon the location of high oscillation. The radial basis functions employing a nine-point grid network are used to improve the functional evaluations by compact formulation, and it saves memory space and computing time. A detailed description of convergence theory is presented to estimate the error bounds. The analysis is based on a strongly connected graph of the Jacobian matrix, and their monotonicity occurred in the scheme. It is shown that the present strategy improves the approximate solution values for the elliptic equations exhibiting a sharp changing character in a thin zone. Numerical simulations for the convection-diffusion equation, Graetz-Nusselt equation, Schrödinger equation, Burgers equation, and Gelfand-Bratu equation are reported to illustrate the utility of the new algorithm.

Keywords. Radial basis function, Compact discretization, Scattered grid network, Schrödinger equation, Gelfand-Bratu equation, Errors.
2010 Mathematics Subject Classification. 65L05, 34K06, 34K28.

1. Introduction

In engineering and sciences, mathematical models present many problems as partial differential equations (PDEs). Simulation of nonlinear elliptic PDEs is the cornerstone of many physical models. It appears in chemical reactions, pattern formation in biology, crystal growth processes, viscous fluid flow, and stationary phenomena. The complex interaction of solutions and parameters to these problems makes it essential for qualitative analysis. The solution of such models helps to understand the quantitative feature of mathematical models. The exact closed-form solution to nonlinear PDEs unravels the complex interaction mechanism among various convection, diffusion, and reaction in steady-state heat and mass transfer processes. The nonlinear PDEs models appearing in acoustics, control theory, optics, fluid dynamics, and other sciences disciplines do not possess exact analytic solutions in general. Thus, the approximation technique for the solution values is famous after the availability of a fast computing machine. It is obtained by employing well-developed mechanisms such as finite-element, finite-volume, spectral method, collocation, spline, wavelets, fuzzy transform, radial basis network, and neural network. With the available stand-alone approximation techniques, each has its advantage in one way. In recent years, hybrid schemes of approximation techniques have been proved more appropriate. The joint application of compact finite-difference discretization and radial basis functions (RBFs) is an elegant approach for numerical approximations to nonlinear PDEs. The classical finite-difference formula is designed on the standard polynomial basis, and it lacks in measuring solutions accurately if considered for the singularly perturbed problems. The discretizing mechanism employing the radial basis function has added an advantage in multidimensions interpolation on scattered data.

Received: 28 April 2022 ; Accepted: 08 February 2023.
∗ Corresponding author. Email: navnitjha@sau.ac.in.

RBFs approximate multivariate functions by considering a simple univariate function and its linear combination. They are considered to estimate functions whose values at a finite number of grids are known and the well-defined procedure can efficiently manage the assessment of the approximating function. RBFs are symmetric, with linearly combined shifted points in Euclidean space to form data-dependent approximations. The dependency on data organizes the application areas more appropriately and approximates a larger class of functions. RBFs' advantages lie in their applicability in higher dimensions because of the small constraints on how the data are prescribed. Also, the high accuracy and faster convergence rate for an approximated target function is an additional reward. The infinitely smooth RBFs are categorized as the global one, and it appears with a shape parameter, where the accuracy and stability of interpolations rely on the shape parameter, Feng and Duan [4]. Various RBFs interpolation on scattered data are presented in recent past, namely Gauss function $\Psi(r) = e^{-(cr)^2}$, thin-plate spline $\Psi(r) = (cr)^2 \log(cr)$, multiquadric $\Psi(r) = \sqrt{1 + (cr)^2}$, inverse quadric $\Psi(r) = 1/[1 + (cr)^2]$, and inverse multiquadric $\Psi(r) = 1/\sqrt{1 + (cr)^2}$. The three-point estimation of ordinary derivatives and approximation of Laplace operator by multiquadric RBFs on scattered and uniform grid points was reported by Bayona et al. [1] and Wright et al. [28]. Application of radial basis functions and finite difference approximations is considered to solve the heat equations, Banei and Shanazari [2]. Tien et al.[26] described an integrated RBFs and compact stencil approach for solving elliptic equations appearing in fluid flow. Jianyu et al.[9] developed an incremental algorithm for multiquadric RBFs and a gradient learning strategy in two-stage for training the net parameters of 2D elliptic PDEs. The method of solution for a two-dimensional cable equation of variable order, Mohebbi et al.[19] and modeling free and forced vibration, Malekzadeh et al. [16] presents an elegant application of RBFs. Fedoseyev et al.[5] discretized nonlinear elliptic PDEs by the multiquadric method and simulated the Gelfand-Bratu equation and Brusselator problem in one- and two-dimensions. In the present work, the two-dimensions singularly perturbed elliptic PDEs with mild nonlinearity are considered

$$\epsilon \left(\partial_x^{(2)} + \partial_y^{(2)}\right) U(x,y) = \phi\left(x, y, U(x,y), \partial_x^{(1)} U(x,y), \partial_y^{(1)} U(x,y)\right), 0 < \epsilon \ll 1, \tag{1.1}$$

where $(x,y) \in \Omega = (a,b) \times (c,d)$, with boundary $\partial\Omega$, along with the Dirichlet boundary data $U(x,y) = \upsilon(x,y)$, $(x,y) \in \partial\Omega$. It appears with a small singular perturbation parameter ϵ, that creates two types of layers, namely horizontal and parallel layers. The computation of such nonlinear problems is cumbersome in the presence of a small parameter, Shishkin et al. [23], Stynes [24]. The assumptions $U(x,y) \in C^4(\Omega)$, continuity of ϕ, and $\partial_U^{(1)} \phi \geq 0$, $\left|\partial_{U^x}^{(1)} \phi\right| \leq K_1$, $\left|\partial_{U^y}^{(1)} \phi\right| \leq K_2$, where $K_1,\ K_2$ are positive constants, ensure the solution uniqueness and existence of the elliptic PDEs (1.1). The approach presented to solve the two-dimensions elliptic PDEs in the present paper implements scattered grid multiquadric radial basis functions (MQ-RBFs) along with minimum stencils compact discretization. The MQ-RBFs technique employs a global basis and is classified as a meshless collocation method with exponential convergence for interpolation problems. We aim to implement only three grid points in each spatial direction to enhance the solution accuracy. We shall describe the algorithm based on the functional values constructed on MQ-RBFs, compact approximation of partial derivatives, and suitable hybridization.

The outline of the article follows the sequence: Section 2 describes the scattered grid network and the associated properties that permit the investigation of the scheme with regard to a single grid parameter. Section 3 will construct partial derivative approximations and compact operators using MQ-RBFs. A high-resolution RBFs compact discretization for Poisson's equation is elaborated in section 4 and extended to nonlinear elliptic PDEs in section 5. The MQ-RBFs combined high-resolution scheme is analyzed for third-order convergence in section 6, and computational illustrations pertaining to l_∞, l_2-errors and convergence rate are reported in section 7. The paper is finally concluded with future scope in section 8.

2. Scattered grid network

Uniform spacing of grids in compact discretization is the simplest, but they are not satisfactory for the problems that exhibit parallel and/or horizontal layer problems, Jha and Kumar [10]. The approximate solution values display gross error in the interior domain if the grid size is not large enough to resolve the parallel or horizontal layer, Ferziger and Peric [6]. The choice of more grid points makes computing time unreasonably high. Implementing scattered grids with continuously varying grid intervals can tackle such a situation if small stencils are considered near the boundary. Let $\{t_l\}_{l=0}^{N+1}$ be the set of uniformly spaced grid points over the domain $[0,1]$ with grid spacing $h = 1/(N+1)$. The computational domain $\bar{\Omega} = [a,b] \times [c,d]$ is populated with the scattered nodes $\{(x_l, y_m)\}$, where

$$x_l = a - (a-b)\, t_l^{n_x}, \quad y_m = c - (c-d)\, t_m^{n_y}, \qquad l, m = 0, \ \cdots, \ \overline{N+1}. \tag{2.1}$$

N is known positive integer, and $n_x,\ n_y$ are positive real numbers, Liu et al. [15]. If $n_x = n_y = 1$, it produces uniformly spaced grid points in the domain Ω. The choice $n_x > 1$, accumulates more grids towards the left whereas $n_x < 1$ results grid cluster towards the right side on the x-axis. A similar observation for $n_y > 1$, $n_y = 1$ or $n_y < 1$ can be interpreted along the y-axis. If $n_x \neq 1$ and $n_y \neq 1$, the unequal spacing among five neighboring grid points $(x_l, y_m), (x_l, y_{m\pm1})$, and $(x_{l\pm1}, y_m)$ can be obtained with the grid step-sizes $h_l = x_l - x_{l-1}, \quad k_m = y_m - y_{m-1}$. Since, grid steps are real numbers, so they are linearly dependent, thus one can choose the subsequent step-size as $h_{l+1} = p_l h_l, \quad k_{m+1} = q_m k_m$. The real numbers p_l and q_m are grid stretching ratios, and their value changes as the computation moves from one stencil to another. The effect of the grid parameters n_x and n_y on the stretching ratio p_l, q_m, and grid points cluster is illustrated as follows. If $n_x = n_y = 1$, the value of stretching ratio p_l and q_m remains fixed and grid points uniformly cover the domain $\bar{\Omega}$. For $n_x, n_y > 1$ the bottom left, and for $n_x, n_y < 1$ upper right concentration to grids are observed. Various combination of grid parameters (a) $n_x = n_y = 0.2$, (b) $n_x = 0.2, \quad n_y = 1.0$, (c) $n_x = 0.2, \quad n_y = 1.8$, (d) $n_x = 1.0, \quad n_y = 0.2$,(e) $n_x = n_y = 1.0$, (f) $n_x = 1.0, \quad n_y = 1.8$, (g) $n_x = 1.8, \quad n_y = 0.2$, (h) $n_x = 1.8, \quad n_y = 1.0$, (i) $n_x = n_y = 1.8$ are considered for illustrating grid concentration in Fig.(1) for $N = 4$ and $\bar{\Omega} = [-1, \ 1]^2$. The variations in grid steps involve a few crucial factors, such as grid stretching ratio and grid smoothness. Therefore, it is essential to note a few observations about the nodal points of the scattered grid network.

Theorem 2.1. *The grid-step sequences $\{h_l\}_{l=1}^{N+1}$ is convergent in $\mathbb{R}$ as $N \to \infty$.*

Proof. The grid-step sequence $\{h_l\}_{l=1}^{N+1}$ is bounded. Since $h_l = x_l - x_{l-1}, l = 1, \cdots, N+1$ and $a \leq x_l \leq b, \quad l = 0, \cdots, \overline{N+1}$ yields $0 < h_l = x_l - x_{l-1} \leq b - a$. Also, using (2.1), we have

$$h_l = (b-a)\left(t_l^{n_x} - t_{l-1}^{n_x}\right) = h^{n_x}(b-a)\left[l^{n_x} - (l-1)^{n_x}\right] > 0, \ \forall l \in \mathbb{Z}_+ \cup \{0\}. \tag{2.2}$$

Depending upon the choice of n_x, three different possibilities arise. If $n_x = 1$, the step-size $h_l = h(b-a)$, and $h_{l+1}/h_l = 1$, for all l. It results in a stationary grid-step sequence. If $n_x > 1$, the sequence $\{h_l\}_{l=1}^{N+1}$is increasing and bounded above, since $h_{l+1}/h_l = \left[(l+1)^{n_x} - l^{n_x}\right]/\left[l^{n_x} - (l-1)^{n_x}\right] > 1, 0 < l \leq \overline{N+1}$. Thus, $\lim \{h_l\}_{l \in \mathbb{Z}_+ \cup \{0\}} = \sup_l \{h_l\}$. For $0 < n_x < 1$, we have $h_{l+1}/h_l = \left[(l+1)^{n_x} - l^{n_x}\right]/\left[l^{n_x} - (l-1)^{n_x}\right] < 1, 0 < l \leq \overline{N+1}$, and $\{h_l\}_{l=1}^{N+1}$ results in a decreasing and bounded below sequence. Therefore, $\lim \{h_l\}_{l \in \mathbb{Z}_+ \cup \{0\}} = \inf_l h_l$. Consequently, the grid-step sequence $\{h_l\}_{l=1}^{N+1}$ is a bounded and monotonic sequence of real numbers for $n_x > 0$. As a result, $\{h_l\}_{l=1}^{N+1}$ and similarly, $\{k_m\}_{m=1}^{N+1}$ is a convergent sequence as $N \to \infty$. $\square$

Theorem 2.2. *The grid stretching rate approaches unity and $\max_{1 \leq l \leq N+1} h_l = 0$, as $N \to \infty$.*

Proof. Let $\varphi : t \longrightarrow x$ be a strictly increasing smooth map in $C^2[0,1]$ satisfying $\varphi(0) = a = x_0, \varphi(1) = b = x_{N+1}$ and $\chi(t) = d\varphi/dt$, such that $\chi'/\chi \in L^\infty[0,1]$. Given a positive integer N, let $t_l = l/(N+1), \quad l = 0, \cdots, \overline{N+1}$, be constant step grids in the domain $[0,1]$. The non-uniform grid sequence $\{x_l\}_{l=0}^{N+1}$ is obtained by setting $\varphi(t_l) = x_l$, $l = 0, \cdots, \overline{N+1}$. Since, $\varphi(t) = x$, we have the differential relation

$$\frac{d\varphi(t)}{dt}\frac{dt}{dx} = 1 \ \Rightarrow dx = \chi(t)dt. \tag{2.3}$$

The relation (2.3) in the discrete form yields $x_l - x_{l-1} \approx \chi(t_{l-1/2})(t_l - t_{l-1})$, that is, $h_l \approx \chi(t_{l-1/2})/(N+1)$. Since $\chi = \varphi', \ \varphi \in C^2[0,1]$, therefore, χ is continuous on the closed interval $[0,1]$, and hence φ is bounded. Thus, $h_l \longrightarrow 0$ for an adequately large value of N. Consequently, $\max_l \ h_l \longrightarrow 0$, as $N \longrightarrow \infty$. Hence, the maximum grid step size diminishes to zero for large enough grid points, Soderlind et al.[22]. This interpretation allows us to analyse the convergence on the scattered grid points in a single parameter N. Further, the grid stretching ratio parameter

$$p_l = \frac{h_{l+1}}{h_l} \approx \frac{\chi\left(t_{l+1/2}\right)}{\chi\left(t_{l-1/2}\right)} = \frac{\chi\left(t_l\right) + \frac{\chi'(t_l)}{2(N+1)} + O\left(\frac{1}{N+1}\right)^2}{\chi\left(t_l\right) - \frac{\chi'(t_l)}{2(N+1)} + O\left(\frac{1}{N+1}\right)^2} = 1 + \frac{1}{N+1}\frac{\chi'\left(t_l\right)}{\chi\left(t_l\right)} + O\left(\frac{1}{N+1}\right)^2. \tag{2.4}$$

Since, $\chi'/\chi \in L^\infty[0,1]$, the space of bounded sequences, the grid step-ratio $p_l \longrightarrow 1$, as $N \longrightarrow \infty$. Therefore, the multiquadric radial basis compact discretization on the scattered grid (2.1) comports a uniform discretization for a large enough value of N. This type of scattered grid topology is more appropriate in the simulations where high accuracy is important, such as boundary layer flow. The dependence between solution values and the spatial grid spacing was described in the past to analyze the electrochemical phenomenon and convection-dominated diffusion problems [3, 11, 12]. □

3. Multiquadric radial basis functions (MQ-RBFs)

Given a set of grid points $\{(x_l, y_m)\}_{l,m=0}^{N+1}$ and corresponding values $U_{l,m} = U\left(x_l, y_m\right)$, the MQ-RBFs is defined as a set of base functions $\{\Psi_{l,m}(x,y)\}_{l,m=0}^{N+1}$, where

$$\Psi_{l,m}(x,y) = \sqrt{1 + c^2||(x,y) - (x_l, y_m)\,||_2^2}, \quad l,m = 0,\cdots,\overline{N+1},$$

and $c > 0$ is a shape parameter. Let $\partial_x^{(1)} = \partial/\partial x,\ \partial_y^{(1)} = \partial/\partial y$ denotes the partial differential operator, and we aim to approximate $\partial_x^{(1)}U(x,y)$ and $\partial_y^{(1)}U(x,y)$ at the four adjoining grid-points $(x_{l\pm1}, y_{m\pm1})$ and one central grid (x_l, y_m), by employing the following three-point relations

$$\partial_x^{(1)}U\left(x_l, y_m\right) \approx \sum_{i=l-1}^{l+1} \alpha_i^{(0)} U\left(x_i, y_m\right), \tag{3.1}$$

and

$$\partial_y^{(1)}U\left(x_l, y_m\right) \approx \sum_{j=m-1}^{m+1} \beta_j^{(0)} U(x_l, y_j). \tag{3.2}$$

The determination of weight coefficients $\alpha_i^{(0)}$ and $\beta_j^{(0)}$, $j = m, m\pm1, i = l, l\pm1$, involves only three-point evaluations in each spatial direction and yields an optimized compact radial basis discretization for the first-order partial differential operators. Replacing the function $U(x,y)$ by radial basis function $\Psi_{i,m}(x,y)$ in the equation (3.1), one obtains

$$\partial_x^{(1)}\Psi_{i,m}(x,y) = \sum_{k=l-1}^{l+1} \alpha_k^{(0)}\Psi_{i,m}(x_k, y_m) = \alpha_l^{(0)}\Psi_{i,m}(x_l, y_m) + \alpha_{l+1}^{(0)}\Psi_{i,m}(x_{l+1}, y_m) + \alpha_{l-1}^{(0)}\Psi_{i,m}(x_{l-1}, y_m). \tag{3.3}$$

For $i = l, l\pm1$, the evaluation of equation (3.3) at $(x,y) = (x_l, y_m)$ yields a system of linear equations

$$\boldsymbol{P}\boldsymbol{\alpha}^{(0)} = \boldsymbol{S}_l. \tag{3.4}$$

Similarly, the relations

$$\partial_x^{(1)}\Psi_{i,m}\left(x_{l+1}, y_m\right) = \alpha_l^{(1)}\Psi_{i,m}\left(x_l, y_m\right) + \alpha_{l+1}^{(1)}\Psi_{i,m}\left(x_{l+1}, y_m\right) + \alpha_{l-1}^{(1)}\Psi_{i,m}(x_{l-1}, y_m), \tag{3.5}$$

and

$$\partial_x^{(1)}\Psi_{i,m}\left(x_{l-1}, y_m\right) = \alpha_l^{(2)}\Psi_{i,m}\left(x_l, y_m\right) + \alpha_{l+1}^{(2)}\Psi_{i,m}\left(x_{l+1}, y_m\right) + \alpha_{l-1}^{(2)}\Psi_{i,m}(x_{l-1}, y_m), \tag{3.6}$$

are evaluated at $(x,y) = (x_{l+1}, y_m)$ and (x_{l-1}, y_m) respectively for $i = l, l\pm1$. It results the following system of equation

$$\boldsymbol{P}\boldsymbol{\alpha}^{(1)} = \boldsymbol{S}_{l+1}, \quad \boldsymbol{P}\boldsymbol{\alpha}^{(2)} = \boldsymbol{S}_{l-1}. \tag{3.7}$$

The MQ-RBFs approximation to partial derivatives along y-space is obtained using

$$\partial_y \Psi_{l,j}(x,y) = \beta_m^{(0)} \Psi_{l,j}(x_l, y_m) + \beta_{m+1}^{(0)} \Psi_{l,j}(x_l, y_{m+1}) + \beta_{m-1}^{(0)} \Psi_{l,j}(x_l, y_{m-1}). \tag{3.8}$$

For $j = m, m \pm 1$, the evaluation of equation (3.8) at $(x,y) = (x_l, y_m)$ yields a system of linear equations

$$\boldsymbol{Q}\boldsymbol{\beta}^{(0)} = \boldsymbol{R}_m. \tag{3.9}$$

Similarly, the relations

$$\partial_y^{(1)} \Psi_{l,j}(x_l, y_{m+1}) = \beta_m^{(1)} \Psi_{l,j}(x_l, y_m) + \beta_{m+1}^{(1)} \Psi_{l,j}(x_l, y_{m+1}) + \beta_{m-1}^{(1)} \Psi_{l,j}(x_l, y_{m-1}), \tag{3.10}$$

and

$$\partial_y^{(1)} \Psi_{l,j}(x_l, y_{m-1}) = \beta_m^{(2)} \Psi_{l,j}(x_l, y_m) + \beta_{m+1}^{(2)} \Psi_{l,j}(x_l, y_{m+1}) + \beta_{m-1}^{(2)} \Psi_{l,j}(x_l, y_{m-1}), \tag{3.11}$$

are evaluated at $(x,y) = (x_l, y_{m+1})$ and $(x,y) = (x_l, y_{m-1})$ respectively for $j = m, m \pm 1$. It yields the following system of equation

$$\boldsymbol{Q}\boldsymbol{\beta}^{(1)} = \boldsymbol{R}_{m+1}, \quad \boldsymbol{Q}\boldsymbol{\beta}^{(2)} = \boldsymbol{R}_{m-1}. \tag{3.12}$$

The weight coefficients can be easily obtained from the equations (3.4), (3.7), (3.9), and (3.12). The associated matrix and vector are as follows

$$\boldsymbol{P} = \begin{bmatrix} \Psi_{l,m}(x_l, y_m) & \Psi_{l,m}(x_{l+1}, y_m) & \Psi_{l,m}(x_{l-1}, y_m) \\ \Psi_{l+1,m}(x_l, y_m) & \Psi_{l+1,m}(x_{l+1}, y_m) & \Psi_{l+1,m}(x_{l-1}, y_m) \\ \Psi_{l-1,m}(x_l, y_m) & \Psi_{l-1,m}(x_{l+1}, y_m) & \Psi_{l-1,m}(x_{l-1}, y_m) \end{bmatrix}, \quad \boldsymbol{S}_l = \begin{bmatrix} \partial_x \Psi_{l,m}(x_l, y_m) \\ \partial_x \Psi_{l+1,m}(x_l, y_m) \\ \partial_x \Psi_{l-1,m}(x_l, y_m) \end{bmatrix},$$

$$\boldsymbol{Q} = \begin{bmatrix} \Psi_{l,m}(x_l, y_m) & \Psi_{l,m}(x_l, y_{m+1}) & \Psi_{l,m}(x_l, y_{m-1}) \\ \Psi_{l,m+1}(x_l, y_m) & \Psi_{l,m+1}(x_l, y_{m+1}) & \Psi_{l,m+1}(x_l, y_{m-1}) \\ \Psi_{l,m-1}(x_l, y_m) & \Psi_{l,m-1}(x_l, y_{m+1}) & \Psi_{l,m-1}(x_l, y_{m-1}) \end{bmatrix}, \quad \boldsymbol{R}_m = \begin{bmatrix} \partial_y \Psi_{l,m}(x_l, y_m) \\ \partial_y \Psi_{l,m+1}(x_l, y_m) \\ \partial_y \Psi_{l,m-1}(x_l, y_m) \end{bmatrix},$$

and for $i, j = 0, 1, 2$:

$$\boldsymbol{S}_{l\pm1} = \begin{bmatrix} \partial_x \Psi_{l,m}(x_{l\pm1}, y_m) \\ \partial_x \Psi_{l+1,m}(x_{l\pm1}, y_m) \\ \partial_x \Psi_{l-1,m}(x_{l\pm1}, y_m) \end{bmatrix}, \ \boldsymbol{R}_{m\pm1} = \begin{bmatrix} \partial_y \Psi_{l,m}(x_l, y_{m\pm1}) \\ \partial_y \Psi_{l,m+1}(x_l, y_{m\pm1}) \\ \partial_y \Psi_{l,m-1}(x_l, y_{m\pm1}) \end{bmatrix}, \ \boldsymbol{\alpha}^{(i)} = \begin{bmatrix} \alpha_l^{(i)} \\ \alpha_{l+1}^{(i)} \\ \alpha_{l-1}^{(i)} \end{bmatrix}, \ \boldsymbol{\beta}^{(j)} = \begin{bmatrix} \beta_m^{(j)} \\ \beta_{m+1}^{(j)} \\ \beta_{m-1}^{(j)} \end{bmatrix}.$$

A similar procedure was applied to obtain the weight coefficients associated with the approximations of second-order partial differentials by defining

$$\partial_x^{(2)} \Psi_{i,m}(x,y) = \sum_{k=l-1}^{l+1} \alpha_k^{(3)} \Psi_{i,m}(x_k, y_m), \tag{3.13}$$

$$\partial_y^{(2)} \Psi_{l,j}(x,y) = \sum_{k=m-1}^{m+1} \beta_k^{(3)} \Psi_{l,j}(x_l, y_k). \tag{3.14}$$

Appendix 1-3 presents the weight coefficients in second-order partial derivatives using equations (3.13) and (3.14) upon employing the MQ-RBF $\Psi_{l,m}(x,y)$. We shall adopt the symbolic representations

$$\left[\partial_x^{(1)} U, \partial_y^{(1)} U, \partial_x^{(2)} U, \partial_y^{(2)} U\right]_{(x,y)=(x_l,y_m)} = \left[U_{l,m}^x, U_{l,m}^y, U_{l,m}^{xx}, U_{l,m}^{yy}\right].$$

Theorem 3.1. *The MQ-RBF approximations of first-order partial derivatives are $O(h_l^2)$-accurate on a scattered grid network.*

Proof. Equation (3.1) and (3.2) gives the approximations of first-order partial derivatives as

$$\begin{bmatrix} \overline{U}_{l,m+\gamma}^x \\ \overline{U}_{l+1,m+\gamma}^x \\ \overline{U}_{l-1,m+\gamma}^x \end{bmatrix} = \boldsymbol{A} \begin{bmatrix} U_{l,m+\gamma} \\ U_{l+1,m+\gamma} \\ U_{l-1,m+\gamma} \end{bmatrix}, \quad \begin{bmatrix} \overline{U}_{l+\gamma,m}^y \\ \overline{U}_{l+\gamma,m+1}^y \\ \overline{U}_{l-\gamma,m-1}^y \end{bmatrix} = \boldsymbol{B} \begin{bmatrix} U_{l+\gamma,m} \\ U_{l+\gamma,m+1} \\ U_{l-\gamma,m-1} \end{bmatrix}, \quad \gamma = 0, \pm1, \tag{3.15}$$

where

$$\boldsymbol{A}=\begin{bmatrix}\alpha_l^{(0)} & \alpha_{l+1}^{(0)} & \alpha_{l-1}^{(0)}\\ \alpha_l^{(1)} & \alpha_{l+1}^{(1)} & \alpha_{l-1}^{(1)}\\ \alpha_l^{(2)} & \alpha_{l+1}^{(2)} & \alpha_{l-1}^{(2)}\end{bmatrix},\quad \boldsymbol{B}=\begin{bmatrix}b_m^{(0)} & b_{m+1}^{(0)} & b_{m-1}^{(0)}\\ b_m^{(1)} & b_{m+1}^{(1)} & b_{m-1}^{(1)}\\ b_m^{(2)} & b_{m+1}^{(2)} & b_{m-1}^{(2)}\end{bmatrix}.$$

Assuming U is $C^4(\Omega)$ continuous function in the neighborhood of the grid-point (x_l, y_m). Then, Taylor's expansions yields

$$\begin{bmatrix}\overline{U}_{l,m}^{x}\\ \overline{U}_{l,m}^{y}\end{bmatrix}=\begin{bmatrix}\left(\partial_x^{(1)}U\right)_{(x_l,y_m)}\\ \left(\partial_y^{(1)}U\right)_{(x_l,y_m)}\end{bmatrix}+\frac{1}{6}\begin{bmatrix}p_l h_l^2\left(3c^2U_{l,m}^{x}+U_{l,m}^{xxx}\right)\\ q_m k_m^2\left(3c^2U_{l,m}^{y}+U_{l,m}^{yyy}\right)\end{bmatrix}+\begin{bmatrix}O\left(h_l^3\right)\\ O\left(k_m^3\right)\end{bmatrix}, \tag{3.16}$$

and

$$\begin{bmatrix}\overline{U}_{l,m\pm1}^{x}\\ \overline{U}_{l\pm1,m}^{y}\end{bmatrix}=\begin{bmatrix}\left(\partial_x^{(1)}U\right)_{(x_l,y_{m\pm1})}\\ \left(\partial_y^{(1)}U\right)_{(x_{l\pm1},y_m)}\end{bmatrix}+\begin{bmatrix}O\left(h_l^2\right)\\ O\left(k_m^2\right)\end{bmatrix}. \tag{3.17}$$

□

Theorem 3.2. *The MQ-RBFs approximations of second-order partial derivatives $\partial_x^{(2)}U$ and $\partial_y^{(2)}U$ are first-order accurate on the scattered grid network and second-order accurate on uniformly spaced grids.*

Proof. The MQ-RBFs approximations (3.13) and (3.14) can be expressed as

$$\overline{U}_{l,m+\gamma}^{xx}=\alpha_l^{(3)}U_{l,m+\gamma}+\alpha_{l+1}^{(3)}U_{l+1,m+\gamma}+\alpha_{l-1}^{(3)}U_{l-1,m+\gamma}, \tag{3.18}$$

$$\overline{U}_{l+\gamma,m}^{yy}=\beta_m^{(3)}U_{l+\gamma,m}+\beta_{m+1}^{(3)}U_{l+\gamma,m+1}+\beta_{m-1}^{(3)}U_{l+\gamma,m-1},\quad \gamma=0,\pm1. \tag{3.19}$$

Application of Taylor's theorem gives

$$\left|\overline{U}_{l,m}^{xx}-\left(\partial_x^{(2)}U\right)_{(x_l,y_m)}\right|=\frac{h_l}{3}(p_l-1)\left(3c^2U_{l,m}^{x}+U_{l,m}^{xxx}\right)+O\left(h_l^2\right), \tag{3.20}$$

and

$$\left|\overline{U}_{l,m}^{yy}-\left(\partial_y^{(2)}U\right)_{(x_l,y_m)}\right|=\frac{k_m}{3}(q_m-1)\left(3c^2U_{l,m}^{y}+U_{l,m}^{yyy}\right)+O\left(k_m^2\right). \tag{3.21}$$

The choice $p_l=q_m=1,\ \forall l,m$ generates the uniform spacing, and the equations (3.20) and (3.21) results in $O\left(h_l^2\right)$ and $O\left(k_m^2\right)$ accuracy respectively. On the other hand, $p_l\neq 1$ and $q_m\neq 1$ populate the grids unevenly, and (3.20)-(3.21) results in $O(h_l)$ and $O\left(k_m\right)$ accuracy. □

Remark 3.3. With the help of approximations (3.15), (3.18), and (3.19), one can define the radial basis compact operators

$$\delta_x^{(1)}U_{l,m}=h_l\overline{U}_{l,m}^{x},\qquad \delta_x^{(2)}U_{l,m}=h_l^2\overline{U}_{l,m}^{xx},\ \delta_y^{(1)}U_{l,m}=k_m\overline{U}_{l,m}^{y},\qquad \delta_y^{(2)}U_{l,m}=k_m^2\overline{U}_{l,m}^{yy}. \tag{3.22}$$

For $c>0$, we can easily estimate

$$\begin{aligned}\delta_x^{(1)}U_{l,m}&=h_lU_{l,m}^{x}+O\left(h_l^2\right),\quad \delta_y^{(1)}U_{l,m}=k_mU_{l,m}^{y}+O\left(k_m^2\right),\\ \delta_x^{(2)}U_{l,m}&=h_l^2U_{l,m}^{xx}+O\left(h_l^3\right),\quad \delta_y^{(2)}U_{l,m}=k_m^2U_{l,m}^{yy}+O\left(k_m^3\right).\end{aligned} \tag{3.23}$$

We have chosen only three grid points in each spatial direction for the radial basis discretization to second and first-order partial derivatives because more than three grid points results in a sparse matrix with large condition numbers and may result in computational instability. Considering a minimum grid-point for discretizing the highest order partial derivative present in elliptic PDEs offers a compact formulation.

4. High-resolution MQ-RBFs compact discretization for Poisson's equation

We shall use MQ-RBFs compact operators $\delta_x^{(k)}$, $\delta_y^{(k)}$ to describe a five-point scheme for solving Poisson's equation

$$\epsilon\left(\partial_x^{(2)}+\partial_y^{(2)}\right)U=\phi\left(x,y\right), \tag{4.1}$$

and later the scheme will be extended to elliptic PDEs (1.1) appearing with nonlinear convection term. Consider the following linear combination

$$\mathcal{L}(h_l,k_m)=h_l^2k_m^2\left(\phi_{l,m}+h_le_{10}\phi_{l,m}^x+k_me_{01}\phi_{l,m}^y+h_l^2e_{20}\phi_{l,m}^{xx}+k_m^2e_{02}\phi_{l,m}^{yy}+h_lk_me_{11}\phi_{l,m}^{xy}\right). \tag{4.2}$$

Using equation (4.1) and MQ-RBFs compact operators (3.22) and (3.23) along with their composite, one obtains

$$\begin{aligned}\mathcal{L}(h_l,k_m)=&\epsilon\bar{\nabla}_{l,m}^2U_{l,m}+\frac{\epsilon h_l^2k_m^2}{3}\left[h_l\left(3e_{10}-p_l+1\right)U_{l,m}^{xxx}+k_m\left(3e_{01}-q_m+1\right)U_{l,m}^{yyy}\right]\\&+\frac{\epsilon h_l^2k_m^2}{12}\left[h_l^2\left(12e_{20}-p_l^2+p_l-1\right)U_{l,m}^{xxxx}+k_m^2\left(12e_{02}-q_m^2+q_m-1\right)U_{l,m}^{yyyy}\right]\\&+\frac{\epsilon h_l^3k_m^3}{3}\left[\left(3e_{11}-(p_l-1)e_{01}\right)U_{l,m}^{xxxy}+\left(3e_{11}-(q_m-1)e_{10}\right)U_{l,m}^{xyyy}\right],\end{aligned} \tag{4.3}$$

where

$$\bar{\nabla}_{l,m}^2=C_{20}\delta_x^{(2)}+C_{02}\delta_y^{(2)}+C_{21}\delta_x^{(2)}\delta_y^{(1)}+C_{12}\delta_x^{(1)}\delta_y^{(2)}+C_{11}\delta_x^{(1)}\delta_y^{(1)}+C_{10}\delta_x^{(1)}+C_{01}\delta_y^{(1)}+C_{22}\delta_x^{(2)}\delta_y^{(2)}-C_{00},$$

and

$$\begin{aligned}&C_{00}=h_l^2k_m^2c^4\left[\left(p_l^2-5p_l+1\right)h_l^2+\left(q_m^2-5q_m+1\right)k_m^2\right]/4,\quad C_{22}=h_l^2e_{20}+k_m^2e_{02},\\&C_{12}=h_l^2e_{10},\quad C_{11}=h_l^2k_m^2c^2\left[\left(1-p_l\right)e_{01}+\left(1-q_m\right)e_{10}\right],\quad C_{10}=h_l^2k_m^2c^2\left(1-p_l\right),\\&C_{20}=k_m^2\left(1-c^2h_l^2p_l\right),\quad C_{01}=h_l^2k_m^2c^2\left(1-q_m\right),\quad C_{02}=h_l^2\left(1-c^2k_m^2q_m\right),\quad C_{21}=k_m^2e_{01}.\end{aligned}$$

The MQ-RBFs compact operator formulation requires the expression of linear combination free from partial differentials. Thus, equating to zero, the coefficients of partial derivatives of $U(x,y)$ at the grid-point (x_l,y_m) in (4.3), one can estimate the values of $e_{i,j}, i,j=0,1,2$. By this way, we find

$$\begin{aligned}&e_{10}=\frac{1}{3}\left(p_l-1\right),\quad e_{01}=\frac{1}{3}\left(q_m-1\right),\quad e_{11}=\frac{1}{9}\left(q_m-1\right)\left(p_l-1\right),\\&e_{20}=\frac{1}{12}\left(p_l^2-p_l+1\right),\quad e_{02}=\frac{1}{12}\left(q_m^2-q_m+1\right),\end{aligned} \tag{4.4}$$

and now the relation (4.3) involves terms of compact operators only. Also, the partial derivatives of $\phi(x,y)$ in the linear combination (4.2) can easily be replaced in terms of MQ-RBFs compact operators and it turns out to be

$$\begin{aligned}\phi_{l,m}^x=&h_l^{-1}\delta_x^{(1)}\phi_{l,m},\quad \phi_{l,m}^y=k_m^{-1}\delta_y^{(1)}\phi_{l,m},\quad \phi_{l,m}^{xy}=h_l^{-1}k_m^{-1}\delta_x^{(1)}\delta_y^{(1)}\phi_{l,m},\\&\phi_{l,m}^{xx}=h_l^{-2}\delta_x^{(2)}\phi_{l,m},\quad \phi_{l,m}^{yy}=k_m^{-2}\delta_y^{(2)}\phi_{l,m}.\end{aligned} \tag{4.5}$$

The compact operator replacement in (4.2), upon using (4.5) yields

$$\mathcal{L}(h_l,k_m)=h_l^2k_m^2\sum_{(i,j)\in\mathcal{S}}G_{i,j}\phi_{i,j}+h_l^2k_m^2O(h_l+k_m)^3, \tag{4.6}$$

where summation runs over the set $\mathcal{S}=\{l-1,l,l+1\}\times\{m-1,m,m+1\}$, and

$$\begin{aligned}&G_{l,m}=\alpha_l^{(0)}\beta_m^{(0)}h_lk_me_{11}+\alpha_l^{(3)}h_l^2e_{20}+\beta_m^{(3)}k_m^2e_{02}+\alpha_l^{(0)}h_le_{10}+\beta_m^{(0)}k_me_{01}+1,\\&G_{l\pm1,m}=\alpha_{l\pm1}^{(0)}h_l(\beta_m^{(0)}k_me_{11}+e_{10})+\alpha_{l\pm1}^{(3)}h_l^2e_{20},\quad G_{l\pm1,m+1}=\alpha_{l\pm1}^{(0)}\beta_{m+1}^{(0)}h_lk_me_{11},\\&G_{l,m\pm1}=\beta_{m\pm1}^{(0)}k_m(\alpha_l^{(0)}h_le_{11}+e_{01})+\beta_{m\pm1}^{(3)}k_m^2e_{02},\quad G_{l\pm1,m-1}=\alpha_{l\pm1}^{(0)}\beta_{m-1}^{(0)}h_lk_me_{11}.\end{aligned}$$

Using (4.3) and (4.6), we obtain

$$\epsilon\bar{\nabla}^2_{l,m}U_{l,m} = h_l^2k_m^2\sum_{(i,j)\in\mathcal{S}}G_{i,j}\phi_{i,j} + h_l^2k_m^2O(h_l+k_m)^3. \tag{4.7}$$

Equivalently,

$$\epsilon h_l^{-2}k_m^{-2}\bar{\nabla}^2_{l,m}U_{l,m} = \begin{cases} \sum_{(i,j)\in\mathcal{S}}G_{i,j}\phi_{i,j} + O(h_l+k_m)^3, & p_l \neq 1 \ \vee \ q_m \neq 1, \\ \sum_{(i,j)\in\mathcal{S}}G_{i,j}\phi_{i,j} + O(h_l+k_m)^4, & p_l = 1 \ \wedge \ q_m = 1, c\to 0. \end{cases} \tag{4.8}$$

The scheme (4.8) solves the Poisson's equations approximately with a third-order accuracy on the scattered grid and brings down the accuracy to the fourth-order on uniformly placed grid points. The present formulation respects the influence of only one central and two adjacent grids in each spatial direction, making it compact whose computation is efficient due to a time-memory trade-off.

5. Compact MQ-RBFs discretization for nonlinear elliptic PDEs

The compact MQ-RBFs scheme for estimating the nonlinear elliptic PDEs (1.1) requires functional estimations and their updates at each grid point of the 3×3 network. The functional $\bar{\phi}_{i,j} = \phi\left(x_i, y_i, U_{i,j}, \bar{U}^x_{i,j}, \bar{U}^y_{i,j}\right), \quad (i,j)\in\mathcal{S}$, upon using the MQ-RBFs approximations (3.15) yields

$$\begin{bmatrix}\bar{\phi}_{l,m}\\ \bar{\phi}_{l+1,m}\\ \bar{\phi}_{l-1,m}\end{bmatrix} = \begin{bmatrix}\phi_{l,m}\\ \phi_{l+1,m}\\ \phi_{l-1,m}\end{bmatrix} - \frac{1}{6}\mathcal{P}_1.\boldsymbol{\omega} + \begin{bmatrix}O(h_l+k_m)^3\\ O(h_l+k_m)^3\\ O(h_l+k_m)^3\end{bmatrix}, \tag{5.1}$$

$$\begin{bmatrix}\bar{\phi}_{l,m+1}\\ \bar{\phi}_{l+1,m+1}\\ \bar{\phi}_{l-1,m+1}\end{bmatrix} = \begin{bmatrix}\phi_{l,m+1}\\ \phi_{l+1,m+1}\\ \phi_{l-1,m+1}\end{bmatrix} - \frac{1}{6}\mathcal{P}_2.\boldsymbol{\omega} + \begin{bmatrix}O(h_l+k_m)^3\\ O(h_l+k_m)^3\\ O(h_l+k_m)^3\end{bmatrix}, \tag{5.2}$$

$$\begin{bmatrix}\bar{\phi}_{l,m-1}\\ \bar{\phi}_{l+1,m-1}\\ \bar{\phi}_{l-1,m-1}\end{bmatrix} = \begin{bmatrix}\phi_{l,m-1}\\ \phi_{l+1,m-1}\\ \phi_{l-1,m-1}\end{bmatrix} - \frac{1}{6}\mathcal{P}_3.\boldsymbol{\omega} + \begin{bmatrix}O(h_l+k_m)^3\\ O(h_l+k_m)^3\\ O(h_l+k_m)^3\end{bmatrix}, \tag{5.3}$$

where

$$\mathcal{P}_1 = \begin{bmatrix} -3p_l & -3q_m & -p_l & -q_m\\ 3p_l\left(p_l+1\right) & -3q_m & p_l\left(1+p_l\right) & -q_m\\ 3\left(p_l+1\right) & -3q_m & 1+p_l & -q_m\end{bmatrix},$$

$$\mathcal{P}_2 = \begin{bmatrix} -3p_l & 3q_m\left(q_m+1\right) & -p_l & (q_m+1)q_m\\ 3p_l\left(1+p_l\right) & 3q_m\left(q_m+1\right) & p_l\left(1+p_l\right) & (q_m+1)q_m\\ 3\left(1+p_l\right) & 3q_m\left(q_m+1\right) & 1+p_l & \left(q_m+1\right)q_m\end{bmatrix},$$

$$\mathcal{P}_3 = \begin{bmatrix} -3p_l & 3\left(1+q_m\right) & -p_l & q_m+1\\ 3p_l\left(p_l+1\right) & 3\left(1+q_m\right) & \left(1+p_l\right)p_l & q_m+1\\ 3(p_l+1) & 3\left(1+q_m\right) & 1+p_l & q_m+1\end{bmatrix}, \boldsymbol{\omega} = \begin{bmatrix} c^2h_l^2A_{l,m}U^x_{l,m}\\ c^2k_m^2B_{l,m}U^y_{l,m}\\ h_l^2A_{l,m}U^{xxx}_{l,m}\\ k_m^2B_{l,m}U^{yyy}_{l,m}\end{bmatrix},$$

and $A_{l,m} = \left(\partial^{(1)}_{U^x}\phi\right)_{(x_l,y_m)}, B_{l,m} = \left(\partial^{(1)}_{U^y}\phi\right)_{(x_l,y_m)}$.

Define the additional partial derivative approximations and updating the functional evaluation at the central grid-point using

$$\hat{U}^x_{l,m} = \bar{U}^x_{l,m} + h_l^2\alpha_0\bar{U}^x_{l+1,m} + \alpha_1h_l\left[\bar{\phi}_{l+1,m} - \epsilon\left(\bar{U}^{yy}_{l+1,m} - \bar{U}^{yy}_{l-1,m}\right) - \bar{\phi}_{l-1,m}\right], \tag{5.4}$$

$$\hat{U}^{y}_{l,m} = \bar{U}^{y}_{l,m} + k_m^2\beta_0\bar{U}^{y}_{l,m+1} + \beta_1 k_m\left[\bar{\phi}_{l,m+1} - \epsilon\left(\bar{U}^{xx}_{l,m+1} - \bar{U}^{xx}_{l,m-1}\right) - \bar{\phi}_{l,m-1}\right], \tag{5.5}$$

$$\hat{\phi}_{l,m} = \phi\left(x_l, y_m, U_{l,m}, \hat{U}^{x}_{l,m}, \hat{U}^{y}_{l,m}\right). \tag{5.6}$$

This implies

$$\hat{U}^{x}_{l,m} = U^{x}_{l,m} + h_l^2\left[\left(\alpha_0 + c^2 p_l/2\right)U^{x}_{l,m} + \left\{\alpha_1\epsilon\left(p_l+1\right) + p_l/6\right\}U^{xxx}_{l,m}\right] + O\left(h_l^3\right), \tag{5.7}$$

$$\hat{U}^{y}_{l,m} = U^{y}_{l,m} + k_m^2\left[\left(\beta_0 + c^2 q_m/2\right)U^{y}_{l,m} + \left\{\beta_1\epsilon\left(q_m+1\right) + q_m/6\right\}U^{yyy}_{l,m}\right] + O\left(k_m^3\right), \tag{5.8}$$

and

$$\begin{aligned}\hat{\phi}_{l,m} =&\phi_{l,m} + \frac{1}{2}A_{l,m}\left(c^2 p_l + 2\alpha_0\right)h_l^2 U^{x}_{l,m} + \frac{1}{2}B_{l,m}\left(c^2 q_m + 2\beta_0\right)k_m^2 U^{y}_{l,m} + \\ &\frac{1}{6}A_{l,m}(6\alpha_1\epsilon(p_l+1) + p_l)h_l^2 U^{xxx}_{l,m} + \frac{1}{6}B_{l,m}\left(6\beta_1\epsilon\left(q_m+1\right) + q_m\right)k_m^2 U^{yyy}_{l,m} + O\left(h_l + k_m\right)^3.\end{aligned} \tag{5.9}$$

Now, employing (5.1)-(5.3) and (5.9) in (4.8) for the modified functional values, we find

$$\sum_{i,j\in\mathcal{S}} G_{i,j}\phi_{i,j} - \sum_{i,j\in\widetilde{\mathcal{S}}} G_{i,j}\bar{\phi}_{i,j} - G_{l,m}\ \hat{\phi}_{l,m} = -\frac{h_l^2 k_m^2}{36 p_l q_m}\left[\zeta_1 h_l^2 A_{l,m} + \zeta_2 k_m^2 B_{l,m}\right] + O(h_l + k_m)^7, \tag{5.10}$$

where

$$\zeta_1 = \left\{2\epsilon\left(p_l+1\right)\zeta\alpha_1 + p_l q_m\left(p_l^2 + p_l + 1\right)\right\}U^{xxx}_{l,m} + \left\{2\zeta\alpha_0 + 3c^2 p_l q_m\left(p_l^2 + p_l + 1\right)\right\}U^{x}_{l,m},$$

$$\zeta_2 = \left\{2\epsilon\left(q_m+1\right)\zeta\beta_1 + p_l q_m\left(q_m^2 + q_m + 1\right)\right\}U^{yyy}_{l,m} + \left\{2\zeta\beta_0 + 3c^2 p_l q_m\left(q_m^2 + q_m + 1\right)\right\}U^{y}_{l,m},$$

and

$$\zeta = 2\left(1 + p_l q_l\right)^2 - \left(q_m + p_l\right)\left(p_l q_m - 2\left(q_m + p_l\right) + 1\right), \quad \widetilde{\mathcal{S}} = \mathcal{S} \sim (l,m).$$

Upon equating the coefficients of $U^{x}_{l,m}, U^{y}_{l,m}, U^{xxx}_{l,m}$ and $U^{yyy}_{l,m}$ in (5.10) to zero, we can eliminate the lower order terms, and it leads to the following values of undetermined coefficients

$$\alpha_0 = -3c^2 p_l q_m\left(p_l^2 + p_l + 1\right)/(2\zeta),\ \ \alpha_1 = -p_l q_m\left(p_l^2 + p_l + 1\right)/2\epsilon\zeta(p_l+1),$$

$$\beta_0 = -3c^2 p_l q_m\left(q_m^2 + q_m + 1\right)/(2\zeta),\ \ \beta_1 = -p_l q_m\left(q_m^2 + q_m + 1\right)/2\epsilon\zeta(q_m+1).$$

As a result, the MQ-RBFs compact discretization is obtained as

$$\epsilon\bar{\nabla}^2_{l,m}U_{l,m} = h_l^2 k_m^2\left[\sum_{i,j\in\widetilde{\mathcal{S}}} G_{i,j}\bar{\phi}_{i,j} + G_{l,m}\ \hat{\phi}_{l,m}\right] + O\left(h_l + k_m\right)^7. \tag{5.11}$$

In the limiting case of radial basis shape parameter c approaching to zero, and $p_l = 1, \quad q_m = 1,\ \forall l, m$. The local truncation error in (5.11) achieves the magnitude $O\left(h_l + k_m\right)^8$.

6. Convergence theory

This section describes the bounds on solution error and convergence theory to the MQ-RBFs compact scheme (5.11) for the elliptic PDEs (1.1). The MQ-RBFs compact scheme (5.11) based on the scattered grid network may be presented as

$$f_{l,m} + O(h_l^7) = 0, \tag{6.1}$$

where

$$f_{l,m} = \epsilon \Big[C_{20}\delta_x^{(2)} + C_{21}\delta_x^{(2)}\delta_y^{(1)} + C_{02}\delta_y^{(2)} + C_{12}\delta_x^{(1)}\delta_y^{(2)} + C_{11}\delta_x^{(1)}\delta_y^{(1)} + C_{10}\delta_x^{(1)} + C_{22}\delta_x^{(2)}\delta_y^{(2)} + C_{01}\delta_y^{(1)} - C_{00}\Big] U_{l,m} - h_l^4\lambda_{l,m}^2 \left[\sum_{i,j\in\widetilde{\mathcal{S}}} G_{i,j}\bar{\phi}_{i,j} + G_{l,m}\ \hat{\phi}_{l,m}\right]. \tag{6.2}$$

One can write the difference equations (6.1) in the vector and matrix form in the following manner

$$\boldsymbol{f}(\boldsymbol{U}) + \boldsymbol{H} = \boldsymbol{0}, \tag{6.3}$$

where $\boldsymbol{U} = [U_{11}, U_{21}, \cdots, U_{N1}, \cdots\cdots, U_{1N}, U_{2N}, \cdots, U_{N^2}]^T$, is the exact solution vector, $\boldsymbol{H} = [H_{11}, H_{21}, \cdots, H_{N1}, \cdots\cdots, H_{1N}, H_{2N}, \cdots, H_{N^2}]^T$ defines the local truncation error vector of seventh-order. Let $\boldsymbol{f(U)} = [f_{11}, f_{21}, \cdots, f_{N1}, \cdots\cdots, f_{1N}, f_{2N}, \cdots, f_{N^2}]^T$. We aim to calculate the approximate value $\boldsymbol{u}$ associated with the exact solution $\boldsymbol{U}$. This can be accomplished by computing the system of nonlinear discretized equation

$$\boldsymbol{f}(\boldsymbol{u}) = \boldsymbol{0}_{N^2\times N^2}. \tag{6.4}$$

Now, in view of the equations (6.3) and (6.4), we get

$$\boldsymbol{f}(\boldsymbol{u}) - \boldsymbol{f}(\boldsymbol{U}) = \boldsymbol{H}. \tag{6.5}$$

Let $\epsilon_{l,m} = u_{l,m} - U_{l,m}$ be the solution error (point-wise) and $\boldsymbol{\epsilon} = [\epsilon_{11}, \epsilon_{21}, \cdots, \epsilon_{N1}, \cdots\cdots, \epsilon_{1N}, \epsilon_{2N}, \cdots, \epsilon_{N^2}]^T$ be the transpose of the error incurred in the MQ-RBF discretization. Now, construct the functional approximation

$$\bar{\varphi}_{j,s} = \phi(x_j, y_s, u_{j,s}, \bar{u}_{j,s}^x, \bar{u}_{j,s}^y) \approx \bar{\phi}_{j,s},, \quad (j,s) \in \bar{\mathcal{S}}, \tag{6.6}$$

and

$$\bar{\varphi}_{l,m} = \phi\left(x_l, y_m, u_{l,m}, \hat{u}_{l,m}^x, \hat{u}_{l,m}^y\right) \approx \bar{\phi}_{l,m}, \qquad \widetilde{D}_{j,s} = \bar{\varphi}_{j,s} - \bar{\phi}_{j,s},\ (j,s) \in \mathcal{S}. \tag{6.7}$$

Employing the Mean value theorem, we find

$$\widetilde{D}_{j,s} = d_{j,s}\bar{\epsilon}_{j,s}^x + e_{j,s}\bar{\epsilon}_{j,s}^y + g_{j,s}\epsilon_{j,s}, \qquad (j,s) \in \bar{\mathcal{S}}, \tag{6.8}$$

where $d_{j,s}$, $e_{j,s}$ and $g_{j,s}$ are real constants and $\bar{\epsilon}_{j,s}^x$, $\bar{\epsilon}_{j,s}^y$ are formulated using the equations (3.15) upon simply interchanging U with ϵ. In a similar manner, $\hat{\epsilon}_{l,m}^x$ and $\hat{\epsilon}_{l,m}^y$ can be obtained from equations (5.5) and (5.6). As a consequence, we may put the discrete equation for solution errors in the following manner

$$\boldsymbol{f}(\boldsymbol{u}) - \boldsymbol{f}(\boldsymbol{U}) = \left[\epsilon h_l^{-2}\bar{\nabla}_{l,m}^2 U_{l,m} - \lambda_{l,m}^2 h_l^2 \left(\sum_{i,j\in\widetilde{\mathcal{S}}} G_{i,j}\bar{\phi}_{i,j} + G_{l,m}\ \hat{\phi}_{l,m}\right)\right], \quad l,m = 1\,(1)\,N. \tag{6.9}$$

In the matrix form, one finds

$$\boldsymbol{f}(\boldsymbol{u}) - \boldsymbol{f}(\boldsymbol{U}) = \boldsymbol{T\epsilon}, \tag{6.10}$$

where $\boldsymbol{T} = [T_{i,j}]$, $\quad i,j = 1, \cdots, N^2$ is the matrix with tri-diagonal blocks. The matrix $\boldsymbol{T}$ consists of all zero elements except at the following locations

for $j = 2(1)N$:

$$T_{(j-1)N+l,N(j-2)-1+l} = \frac{\epsilon\{\lambda_{l,j}^2(q_j^2 - q_j - 1) + p_l^2 - p_l - 1\}}{3\,(q_j+1)\,(p_l+1)} + O\,(h_l)\,,\ l = 2, \cdots, N,$$

$$T_{(j-1)N+l,N(j-2)+l} = -\frac{\epsilon\{\lambda_{l,j}^2(q_j^2 - q_j - 1) + p_l^2 + 3p_l + 1\}}{3p_l\,(q_j + 1)} + O\,(h_l)\,,\ l = 1, \cdots, N,$$

$$T_{(j-1)N+l,(j-2)N+1+l} = \frac{\epsilon\{\lambda_{l,j}^2(q_j^2 - q_j - 1) - p_l^2 - p_l + 1\}}{3\,(q_j + 1)\,p_l\,(p_l + 1)} + O\,(h_l)\,, l = 1, \cdots, N-1,$$

for $j = 1(1)N$:

$$T_{(j-1)N+l,N(j-2)-1+l} = -\frac{\epsilon\{\lambda_{l,j}^2(q_j^2 + 3q_j + 1) + p_l^2 - p_l - 1\}}{3q_j\,(p_l + 1)} + O\,(h_l)\,,\ l = 2, \cdots, N,$$

$$T_{(j-1)N+l,N(j-2)+l} = \frac{\epsilon\{\lambda_{l,j}^2(q_j^2 + 3q_j + 1) + p_l^2 + 3p_l + 1\}}{3p_l q_j} + O\,(h_l)\,,\ l = 1, \cdots, N,$$

$$T_{(j-1)N+l,(j-2)N+1+l} = -\frac{\epsilon\{\lambda_{l,j}^2(q_j^2 + 3q_j + 1) - p_l^2 - p_l + 1\}}{3p_l q_j\,(p_l + 1)} + O\,(h_l)\,,\ l = 1, \cdots, N-1,$$

for $j = 1(1)N-1$:

$$T_{(j-1)N+l,(j-2)N+l-1} = -\frac{\epsilon\{\lambda_{l,j}^2(q_j^2 + q_j - 1) - p_l^2 + p_l + 1\}}{3q_j\,(q_j + 1)\,(p_l + 1)} + O\,(h_l)\,,\ l = 2, \cdots, N,$$

$$T_{N(j-1)+l,N(j-2)+l} = \frac{\epsilon\{\lambda_{l,j}^2(q_j^2 + q_j - 1) - p_l^2 - 3p_l - 1\}}{3q_j\,(q_j + 1)\,p_l} + O\,(h_l)\,,\ l = 1, \cdots, N,$$

$$T_{l+(j-1)N,(j-2)N+1+l} = -\frac{\epsilon\{\lambda_{l,j}^2(q_j^2 + q_j - 1) + p_l^2 + p_l - 1\}}{3q_j\,(q_j + 1)\,p_l\,(p_l + 1)} + O\,(h_l)\,,\ l = 1, \cdots, N-1.$$

From the equations (6.5) and (6.10), we have

$$\boldsymbol{T\epsilon} = \boldsymbol{H}. \tag{6.11}$$

For the significantly diminishing values of grid steps h_l and $0 < p_l, q_m \neq (\sqrt{5} \pm 1)/2$, it appears that upper, principal, and lower tri-diagonal blocks results in non-vanishing values at sub-diagonal and main diagonal. Also, there exists a finite length walk $(i \to i_1), (i_1 \to i_2), \cdots, (i_n \to j)$ that joins ordered pair vertex i and j, depicted on a plane corresponding to nonzero elements $T_{i,j}$ of matrix $\boldsymbol{T}$. This establishes the strongly connected feature to the graph $\boldsymbol{\mathcal{G}}(\boldsymbol{T})$. Consequently, the matrix $\boldsymbol{T}$ is irreducible, Young [29], Varga [27]. The directed graph can be visualized for a specific value (say) $N = 3$ in Figure 1. Let $d = \min\limits_{i,j} d_{i,j}$, $e = \min\limits_{i,j} e_{i,j}$, $g = \min\limits_{i,j} g_{i,j}$, $\underline{p} = \min\limits_{l} p_l$, $\underline{q} = \min\limits_{m} q_m$, $\bar{\lambda} = \max\limits_{i,j} \lambda_{i,j}$ and $\underline{\lambda} = \min\limits_{i,j} \lambda_{i,j}$. Let θ_s represents the sum of elements in s^{th} row of the matrix $\boldsymbol{T}$. Thus , for $h_l \to 0^+$ and $(\sqrt{5} - 1)/2 < p_l, q_m < (\sqrt{5} + 1)/2$, it is easy to estimate the following

$$\theta_1 \geq \frac{\epsilon\{\underline{p}^2 + 5\underline{p} + 5 + \underline{\lambda}^2(\underline{q}^2 + 5\underline{q} + 5)\}}{3(\underline{q} + 1)(\underline{p} + 1)} > 0,$$

$$\theta_s \geq \frac{2\epsilon}{(\underline{q} + 1)} > 0, \quad s = 2, ..., N-1,$$

$$\theta_N \geq \frac{\epsilon\{5\underline{p}^2 + 5\underline{p} + 1 + \underline{\lambda}^2(\underline{q}^2 + 5\underline{q} + 5)\}}{3(\underline{q} + 1)(\underline{p} + 1)} > 0,$$

$$\theta_{(r-1)N+1} \geq \frac{2\epsilon\underline{\lambda}^2}{(\underline{p} + 1)} > 0, \quad r = 2, \cdots, N-1,$$

$$\theta_{(r-1)N+s} \geq gh^2\underline{\lambda}^2, \quad r, s = 2, \cdots, N-1, \quad g \geq 0,$$

$$\theta_{(r-1)N+N} \geq \frac{2\epsilon\underline{\lambda}^2}{\underline{p}(\underline{p}+1)} > 0, \quad r = 2, \cdots, N-1,$$
$$\theta_{(N-1)N+1} \geq \frac{\epsilon\{\underline{p}^2 + 5\underline{p} + 5 + \underline{\lambda}^2(5\underline{q}^2 + 5\underline{q} + 1)\}}{(\underline{q}+1)\underline{q}(\underline{p}+1)} > 0,$$
$$\theta_{(N-1)N+s} \geq \frac{2\epsilon}{(1+\underline{q})\underline{q}} > 0, \quad s = 2, \cdots, L-1,$$
$$\theta_{N^2} \geq \frac{\epsilon\{5\underline{p}^2 + 5\underline{p} + 1 + \underline{\lambda}^2(5\underline{q}^2 + 5\underline{q} + 1)\}}{\underline{q}(\underline{q}+1)\underline{p}(\underline{p}+1)} > 0.$$

As a result, $\boldsymbol{T}$ is a monotone matrix. Hence, the matrix $\boldsymbol{T}$ is jointly monotone and irreducible, if $(\sqrt{5}-1)/2 < p_l, q_m < (\sqrt{5}+1)/2$ and $g \geq 0$ (Henrici [7]). As a result, $\boldsymbol{T^{-1}}$ exists, moreover $\boldsymbol{T^{-1}} > \boldsymbol{0}$. Let $T^{-1}_{i,j}$ denote the $(i,j)^{th}$ element of $\boldsymbol{T^{-1}}$. The matrix and vector norm is given by

$$||\boldsymbol{T}^{-1}||_\infty = \max_{k=1(1)N^2}\Bigg[|T^{-1}_{k,1}| + \sum_{s=2}^{N-1}|T^{-1}_{k,s}| + |T^{-1}_{k,L}| + |T^{-1}_{k,(N-1)N+1}| + \sum_{s=2}^{N-1}|T^{-1}_{k,(N-1)N+s}|$$
$$+|T^{-1}_{k,N^2}| + \sum_{s=2}^{N-1}(|T^{-1}_{k,(r-1)N+s}| + \sum_{s=2}^{N-1}|T^{-1}_{k,(r-1)N+s}| + |T^{-1}_{k,rN}|)\Bigg],$$

and

$$||\boldsymbol{H}||_\infty = \max_{l=1(1)N}\sum_{j=1(1)N} H_{l,j}.$$

From the elementary matrix relation $\boldsymbol{T^{-1}}(\boldsymbol{TI}) = \boldsymbol{I}$, where $\boldsymbol{I}$ is the $N^2 \times 1$ matrix having each of its elements are 1, one can find

$$\sum_{j=1(1)N^2} T^{-1}_{k,j}\theta_j = 1, \quad k = 1(1)N^2. \tag{6.12}$$

Employing series expansion, we can easily estimate the upper bounds on the non-zero entries of $\boldsymbol{T^{-1}}$. For $\underline{h} = \min_l h_l$, $\bar{h} = \max_l h_l$ and $j = 1(1)N^2$:

$$T^{-1}_{j,1} \leq \frac{1}{\theta_1} \leq 3(\underline{p}+1)(\underline{q}+1)/[\epsilon\{\underline{p}^2 + 5\underline{p} + 5 + \underline{\lambda}^2(\underline{q}^2 + 5\underline{q} + 5)\}] + O(\bar{h}),$$
$$\sum_{s=2}^{N-1} T^{-1}_{j,s} \leq \frac{1}{\min\limits_{s=2(1)N-1}\theta_s} \leq \frac{(\underline{q}+1)}{(2\epsilon)} + O\left(\bar{h}\right),$$
$$T^{-1}_{j,N} \leq \frac{1}{\theta_N} \leq 3\underline{p}(\underline{p}+1)(\underline{q}+1)/[\epsilon\{5\underline{p}^2 + 5\underline{p} + 1 + \underline{\lambda}^2(\underline{q}^2 + 5\underline{q} + 5)\}] + O(\underline{h}),$$
$$\sum_{r=2(1)N-1} T^{-1}_{j,N(r-1)+1} \leq \frac{1}{\min\limits_{r=2(1)N-1}\theta_{(r-1)N+1}} \leq \frac{(\underline{p}+1)}{(2\epsilon\underline{\lambda}^2)} + O\left(\bar{h}\right),$$
$$\sum_{r=2}^{N-1}\sum_{s=2}^{N-1} T^{-1}_{j,(r-1)N+s} \leq \begin{cases} \sum_{s=1}^{N^2} T^{-1}_{j,s}\theta_s = 1, & g = 0, \\ \frac{1}{\min\limits_{s,r=2(1)N-1}\theta_{(r-1)N+s}} \leq \frac{1}{g\underline{h}^2\underline{\lambda}^2}, & g > 0, \end{cases}$$
$$\sum_{r=2}^{N-1} T^{-1}_{j,rN} \leq \frac{1}{\min\limits_{r=2(1)N-1}\theta_{rN}} \leq \frac{\underline{p}(\underline{p}+1)}{(2\epsilon\underline{\lambda}^2)} + O\left(\bar{h}\right),$$
$$T^{-1}_{j,(N-1)N+1} \leq \frac{1}{\theta_{(N-1)N+1}} \leq 3\underline{q}(\underline{p}+1)(\underline{q}+1)/[\epsilon\{\underline{p}^2 + 5\underline{p} + 5 + \underline{\lambda}^2(5\underline{q}^2 + 5\underline{q} + 1)\}] + O(\underline{h}),$$

$$\sum_{s=2}^{N-1} T^{-1}_{j,(N-1)N+s} \leq \frac{1}{\min\limits_{s=2(1)N-1} \theta_{(N-1)N+s}} \leq \frac{(\underline{q}+1)\underline{q}}{(2\epsilon)} + O\left(\bar{h}\right),$$

$$T^{-1}_{j,N^2} \leq \frac{1}{\theta_{N^2}} \leq 3\underline{p}(\underline{p}+1)\underline{q}(\underline{q}+1)/[\epsilon\{5\underline{p}^2+5\underline{p}+1+\underline{\lambda}^2(5\underline{q}^2+5\underline{q}+1)\}] + O(\underline{h}).$$

Combining above inequalities, one finds

$$||\epsilon||_\infty \leq ||\boldsymbol{T}^{-1}||_\infty.||\boldsymbol{H}||_\infty \leq \begin{cases} \frac{\underline{h}^3}{\underline{g}\underline{\lambda}^2} + O(\underline{h}^5), & \underline{g} > 0, \\ O(\underline{h}^5), & \underline{g} = 0, \end{cases} \tag{6.13}$$

$$\implies ||\epsilon||_\infty \leq \min\left\{ \frac{\underline{h}^3}{\underline{g}\underline{\lambda}^2} + O(\underline{h}^5), O(\underline{h}^5) \right\} = O(\underline{h}^3) \leq O(\underline{h}^3). \tag{6.14}$$

The inequalities (6.13) prove that the quantity $O(\bar{h}^3)$ bounds the maximum point-wise solution error. It invigorate the convergence order of three for the MQ-RBFs combined compact formulation on a scattered grid network. A close observation on the inequality (6.13) shows the restriction $\underline{g} \geq 0$ for the scheme to converge. The term $\underline{g}$ refers to the coefficient $g_{j,s}$ and it denote the point-wise evaluation of $\partial_U^{(1)}\phi$ at the grid (x_j, y_s). Consequently, the condition $\partial_U^{(1)}\phi \geq 0$ supersede with $\underline{g} \geq 0$. The condition $\partial_U^{(1)}\phi \geq 0$ resemble the criterion for the existence and uniqueness of the solution.

7. Numerical simulations and performance measure

The qualities of solution values obtained by MQ-RBFs combined with compact third-order discretization on scattered grids will be compared with the corresponding method on uniformly spaced grid points. The difference equations alongside boundary data bring block-tri-diagonal Jacobian matrix and are effectively computed utilizing Gauss-Seidel formula or Newton-Raphson scheme. The iterative scheme assumes a zero vector as an initial guess, and computation continues till the error tolerance achieves an accuracy of 10^{-12}, Thomas [25], Higham [8]. As a procedure of test case, Dirichlet boundary data is acquired using the analytic solution. We validate the convergence order and solution errors using l_∞ and l_2 norms of the error metrics. These metrics are implemented by using the formula

$$||\epsilon||_2 = \sqrt{\frac{1}{N^2}\sum_{l=1}^{N}\sum_{m=1}^{N}|U_{l,m}-u_{l,m}|^2}, \quad \Theta_2 = \log_2\left(\frac{||\epsilon||_2 : l,m=1(1)N}{||\epsilon||_2 : l,m=1(1)2N}\right), \tag{7.1}$$

$$||\epsilon||_\infty = \max_{1\leq l,m\leq N}|u_{l,m}-U_{l,m}|, \quad \Theta_\infty = \log_2\left(\frac{||\epsilon||_\infty : l,m=1(1)N}{||\epsilon||_\infty : l,m=1(1)2N}\right). \tag{7.2}$$

The solution accuracies in approximate numerical values and exact solutions are obtained for scattered grid ($p_l \neq 1 or\ q_m \neq 1$) and uniform grids ($p_l = q_m = 1$) for different values of MQ-RBFs shape parameter c. The software tool CodeGeneration in Maple 17 is used to obtain nonzero elements of the Jacobian matrix as symbolic computation, and Python 3.7 is considered for numerical computations. Both the computing tools are performed on Mac book 2.6 (Pro) GHz 6-Core, Intel Core i7, Catalina operating system.

Example 7.1. Consider the Graetz-Nusselt equation used to analyze heat transfer between a tube at a constant wall temperature and a developed laminar fluid flow

$$\epsilon\left(\partial_x^{(2)}+\partial_y^{(2)}\right)U\left(x,y\right) = (1-y^2)U\left(x,y\right), \quad -1<x,y<1, \tag{7.3}$$

with the boundary data

$$U\left(-1,y\right) = e^{\epsilon-\frac{y^2}{2}}\Phi\left(-\frac{\epsilon^2}{4},\frac{1}{2},y^2\right), \qquad U\left(1,y\right) = e^{-\epsilon-\frac{y^2}{2}}\Phi\left(-\frac{\epsilon^2}{4},\frac{1}{2},y^2\right),$$

$$U(x,-1)=e^{-\epsilon x-\frac{1}{2}}\Phi\left(-\frac{\epsilon^2}{4},\frac{1}{2},1\right),\qquad U(x,1)=e^{-\epsilon x-\frac{1}{2}}\Phi\left(-\frac{\epsilon^2}{4},\frac{1}{2},1\right).$$

It possesses the theoretical solution

$$U(x,y)=e^{-\epsilon x-\frac{y^2}{2}}\Phi\left(-\frac{\epsilon^2}{4},\frac{1}{2},y^2\right),\quad \Phi(a,b;\zeta)=1+\sum_{n=1}^{\infty}\frac{a(a+1)\cdots(a+n-1)}{b(b+1)\cdots(b+n-1)}\frac{\zeta^n}{n!}. \tag{7.4}$$

Here $\Phi(a,b;\zeta)$ is the degenerate hypergeometric function and $P_e=1/\epsilon$ is the Peclet number, Polyanin [21]. The desired concentration distribution may be designed by generating streams with a known concentration and further overlaying them with the stream at a high Peclet number. The value of the Peclet number sharply affects the solution accuracies and convergence order. If $P_e\geq 1$, the error in exact and approximate solution values appears with fourth-order convergence rate for the shape parameter $c\to 0$ and uniformly distributed grids $n_x=n_y=1$. Simulations with $c=10^{-2}$ and $n_x=n_y=1$ are performed with $P_e=10$ in Table 1 for various grid arrangements. A similar observation for the accurate solution values and proper convergence order is observed for the larger value of the Peclet number. If the advection term is dominant, then the Peclet number will be large, and thus the heat transfer from the wall is less important.

Conversely, the heat transfer from the wall to the fluid can be of higher importance in the case of a smaller Peclet number. The concentration distribution is dominated by diffusion for a low Peclet number. For $P_e=0.1<1$, the solution converges, but accuracies deteriorate with standard discretization in the limiting value of shape parameter $c=10^{-2}$ (say). However, the change in shape parameter values, solution accuracy, and convergence order can be accurately measured while keeping grids' uniformity $n_x=n_y=1$, see Table 2. This shows the importance of changing the value of shape parameters in the radial basis framework. The graphical illustration for a surface plot at $P_e=0.1$ and 10 are presented in Figures 2 and 3, respectively, by employing 64 grid points in each coordinate direction.

Example 7.2. A common practice for experimenting with the algorithm is by means of Poisson's equation that possesses an analytic solution with a steep wavefront inside the solution domain. We shall use a circular wavefront as discussed in Mitchell [17]. The arctangent wavefront leads to the mild singularity at the center of the circle. Values of parameters determine the location and steepness of the wavefront. Poisson's equation

$$\left(\partial_x^{(2)}+\partial_y^{(2)}\right)U(x,y)=\frac{\epsilon\eta\left(1-\eta^2\left(r^2-r_0^2\right)\right)}{r\left(1+\eta^2\left(r-r_0\right)^2\right)^2},\qquad 0<x,y<1, \tag{7.5}$$

with the boundary data

$$\begin{aligned}U(0,y)&=\tan^{-1}\left(\eta\left(\sqrt{x_c^2+(y-y_c^2)^2}-r_0\right)\right),\ U(1,y)=\tan^{-1}\left(\eta\left(\sqrt{(1-x_c)^2+(y-y_c^2)^2}-r_0\right)\right),\\ U(x,0)&=\tan^{-1}\left(\eta\left(\sqrt{(x-x_c^2)^2+y_c^2}-r_0\right)\right),\ U(x,1)=\tan^{-1}\left(\eta\left(\sqrt{(x-x_c)^2+(1-y_c^2)^2}-r_0\right)\right).\end{aligned}$$

It possesses the theoretical solution $U(x,y)=\tan^{-1}(\eta(r-r_0)), r=\sqrt{(x-x_c)^2+(y-y_c)^2}$. Here (x_c,y_c) is the center of the circular wavefront, r_0 is the distance from the center of the circle to the wavefront, and η signifies the wavefront steepness. The point-wise error $\mathcal{E}_{l,m}=|U_{l,m}-u_{l,m}|$ for various values of parameters, (see Table 3) with $N=16$ and $c=0.1$ is obtained in Table 4. In each wavefront, it is essential to employ scattered grids of high-resolution MQ-RBFs to measure the solution values accurately. Figures 4-7 illustrate the variation in a surface plot with a change in values of wavefront parameters.

Example 7.3. (Komech [14]) Consider the linear Schrödinger equation

$$\epsilon\left(\partial_x^{(2)}+\partial_y^{(2)}\right)U(x,y)=(x^2+y^2)U(x,y),\quad 0<x,y<1, \tag{7.6}$$

with the boundary data

$$U(0,y) = 1 - y^2/2, \qquad U(1,y) = \left\{3/2 - y^2/2\right\}\left\{\sinh\left(\epsilon^{-1/2}y\right) + \cosh\left(\epsilon^{-1/2}y\right)\right\},$$
$$U(x,0) = 1 + x^2/2, \qquad U(x,1) = \left\{x^2/2 + 1/2\right\}\left\{\sinh\left(\epsilon^{-1/2}x\right) + \cosh\left(\epsilon^{-1/2}x\right)\right\}.$$

It possesses the theoretical solution

$$U(x,y) = \left\{\left(x^2 - y^2\right)/2 + 1\right\}\left\{\sinh\left(\epsilon^{-1/2}xy\right) + \cosh\left(\epsilon^{-1/2}xy\right)\right\}. \tag{7.7}$$

The norm of solution errors along with the numerical convergence rate for various grid points verify the theoretical deductions. The left side of Table 5 shows the estimated error and convergence rate with uniformly distributed grids and low value of shape parameters. While the right columns in Table 5 show errors and numerical order over nonuniform grids and varying values of radial basis shape parameters. The solution accuracy improves with changing shape parameters and nonuniformity in grids, showing the present formulation's importance.

Example 7.4. (Jha et al. [13]) The linear convection-diffusion equation

$$\epsilon\left(\partial_x^{(2)} + \partial_y^{(2)}\right)U(x,y) = \partial_x^{(1)}U(x,y), \quad -1 < x, y < 1, \tag{7.8}$$

with the boundary data

$$U(-1,y) = e^{\frac{-1}{2\epsilon}}\{2e^{\frac{-1}{2\epsilon}}\sinh(\tau) + \sinh(2\tau)\}\sin(\pi y)\,\text{cosech}(\tau), \qquad U(1,y) = 2\sin(\pi y),$$
$$U(x,-1) = -e^{\frac{x}{2\epsilon}}\{2e^{\frac{-1}{2\epsilon}}\sinh(\tau x) + \sinh(\tau(1-x))\}\sin(\pi)\,\text{cosech}(\tau), \quad U(x,1) = -U(x,-1).$$

It possesses the theoretical solution

$$U(x,y) = e^{\frac{x}{2\epsilon}}\{2e^{\frac{-1}{2\epsilon}}\sinh(\tau x) + \sinh[\tau(1-x)]\}\sin(\pi y)\,\text{cosech}(\tau), \qquad \tau = \frac{1}{2}\sqrt{\frac{1}{\epsilon^2} + 4\pi^2}. \tag{7.9}$$

In the numerical simulation, it is observed that solution errors and convergence order is almost accurate for $\epsilon = 1$, but it deteriorates for $\epsilon = 10^{-1}$ and 10^{-2} with a very low value of shape parameter $c = 0.001$, and uniformly distributed grids $n_x = n_y = 1$, see Table 6. The joint effect of radial basis shape parameter value $c = 0.01$ and variable grid spacing $n_x \neq 1$ or $n_y \neq 1$ measure the solution values more precisely for $\epsilon = 10^{-1}$ and 10^{-2}, see Table 7. Thus, the hybrid scheme employing nonuniformly spaced grids compact discretization with MQ-RBFs is advantageous compared with standard high-resolution scheme of same order.

Example 7.5. Consider the Burgers equation

$$\epsilon\left(\partial_x^{(2)} + \partial_y^{(2)}\right)U(x,y) = U(x,y)\left(\partial_x^{(1)} + \partial_y^{(1)}\right)U(x,y) + g(x,y), \quad 0 < x, y < 1, \tag{7.10}$$

where

$$g(x,y) = -\frac{1}{4}e^x\sin\left(\frac{\pi y}{2}\right)\left[2e^x\left(\pi\cos\left(\frac{\pi y}{2}\right) + 2\sin\left(\frac{\pi y}{2}\right)\right) + \epsilon(\pi^2 - 4)\right],$$

with the boundary data

$$U(0,y) = \sin\left(\frac{\pi y}{2}\right), \qquad U(1,y) = e\sin\left(\frac{\pi y}{2}\right), \qquad U(x,0) = 0, \qquad U(x,1) = e^x.$$

It possesses the theoretical solution

$$U(x,y) = e^x\sin\left(\frac{\pi y}{2}\right).$$

The maximum-absolute error and convergence rate for different grid arrangements are compared with compact exponential approximation (Mohanty et al. [18]) and presented in Table 8 for a small value $\epsilon = 10^{-3}$ using the various grid points.

Example 7.6. (Mohsen [20]) Consider the Gelfand-Bratu equation

$$\epsilon\left(\partial_x^{(2)}+\partial_y^{(2)}\right)U(x,y)+e^{\sigma U(x,y)}=0,\quad \epsilon,\sigma>0,\quad -1<x,y<1. \tag{7.11}$$

It admits two solutions

$$\text{Case-1:}\qquad U(x,y)=\frac{1}{\sigma}\log\left(\frac{4\epsilon}{\sigma\cosh^2(x+y+1)}\right), \tag{7.12}$$

and

$$\text{Case-2:}\qquad U(x,y)=\frac{1}{\sigma}\log\left(\frac{4\epsilon}{\sigma\cosh^2(x-y+1)}\right). \tag{7.13}$$

The boundary data associated with Case-1 are

$$U(0,y)=\frac{1}{\sigma}\log\left(\frac{4\epsilon}{\sigma\cosh^2(y+1)}\right),\qquad U(1,y)=\frac{1}{\sigma}\log\left(\frac{4\epsilon}{\sigma\cosh^2(y+2)}\right), \tag{7.14}$$

$$U(x,0)=\frac{1}{\sigma}\log\left(\frac{4\epsilon}{\sigma\cosh^2(x+1)}\right),\qquad U(x,1)=\frac{1}{\sigma}\log\left(\frac{4\epsilon}{\sigma\cosh^2(x+2)}\right), \tag{7.15}$$

and the boundary data associated with Case-2 are

$$U(0,y)=\frac{1}{\sigma}\log\left(\frac{4\epsilon}{\sigma\cosh^2(y-1)}\right),\qquad U(1,y)=\frac{1}{\sigma}\log\left(\frac{4\epsilon}{\sigma\cosh^2(y-2)}\right), \tag{7.16}$$

$$U(x,0)=\frac{1}{\sigma}\log\left(\frac{4\epsilon}{\sigma\cosh^2(x+1)}\right),\qquad U(x,1)=\frac{1}{\sigma}\log\left(\frac{4\epsilon}{\sigma\cosh^2(x)}\right). \tag{7.17}$$

For $n_x=n_y=1$, $\sigma=6.793248$ and $\epsilon=1$, the solution errors along with convergence order using proposed MQ-RBFs combined high-resolution compact discretization are presented in Table 9 by employing the theoretical solutions (7.12) and (7.13). The solution accuracies and convergence orders are better than the error $||\epsilon||_\infty=2.1e-03$ and $1.6e-05$, compared with the results reported in Fedoseyev et al. [5], that considered the multiquadric method and compared the results with a central-difference second-order scheme and high-order orthogonal spline collocation method. Simulations with sufficiently small values of $\epsilon=\sigma=10^{-5}$ exhibit oscillatory solutions for uniform distribution of grids; however, the choice $n_x=1.04$, $n_y=1$, offer order-preserving solution values.

Table 1. Accuracies of solution error and convergence order for $P_e=1$ and $P_e=10$.

L	$\|\|\epsilon\|\|_2$	Θ_2	$\|\|\epsilon\|\|_\infty$	Θ_∞	$\|\|\epsilon\|\|_2$	Θ_2	$\|\|\epsilon\|\|_\infty$	Θ_∞
	$P_e=1$				$P_e=10$			
8	3.79e-5	—	6.84e-5	—	1.04e-5	—	2.10e-5	—
16	2.78e-6	3.8	5.46e-6	3.6	7.79e-7	3.7	1.71e-6	3.6
32	1.47e-7	4.2	3.14e-7	4.1	5.32e-8	3.9	1.21e-7	3.8
64	1.08e-8	3.9	2.30e-8	4.0	3.17e-9	4.1	7.17e-9	4.1

Table 2. Effect of shape parameter on solution error and convergence order for $P_e=0.1$.

L	c	$\|\|\epsilon\|\|_2$	Θ_2	c	$\|\|\epsilon\|\|_2$	Θ_2
8	0.001	3.02e+01	—	0.72	6.08e-01	—
16	0.001	7.78e-01	5.3	0.37	3.77e-02	4.0
32	0.001	1.48e-02	5.7	0.20	1.89e-03	4.3
64	0.001	2.63e-04	5.8	0.11	1.20e-04	4.1

TABLE 3. Values of wavefront parameters.

Name	η	r_0	x_c	y_c
well	50	0.70	0.50	0.50
asymmetric	1000	0.70	1.50	0.25
steep	1000	0.92	-0.05	-0.05
mild	20	0.25	-0.05	-0.05

TABLE 4. Point-wise solution errors for well, asymmetric, steep and mild cases.

$\eta = 20, \quad r_0 = 0.70, \quad (x_c,\ y_c) = (-0.05,\ -0.05), n_x = 0.8, n_y = 1.0$						
$\mathcal{E}_{l,m}$	7.72e-04	2.63e-03	8.71e-03	2.11e-03	9.35e-04	2.33e-04
x_l, y_m	0.10,0.06	0.17,0.12	0.31,0.24	0.86,0.82	0.90,0.88	0.95,0.94
$\eta = 1000, \quad r_0 = 0.70, \quad (x_c,\ y_c) = (-0.05,\ -0.05), n_x = 0.6, n_y = 0.7$						
$\mathcal{E}_{l,m}$	1.51e-02	1.26e-03	2.29e-03	1.36e-03	5.70e-04	1.35e-04
x_l, y_m	0.73,0.69	0.77,0.74	0.81,0.78	0.89,0.87	0.93,0.92	0.96,0.92
$\eta = 1000, \quad r_0 = 0.92, \quad (x_c,\ y_c) = (1.50,\ 0.25), n_x = 1.2, n_y = 0.3$						
$\mathcal{E}_{l,m}$	5.32e-03	1.51e-02	2.80e-02	4.35e-02	6.20e-02	2.68e-01
x_l, y_m	0.03,0.43	0.08,0.53	0.12,0.59	0.18,0.65	0.23,0.69	0.47,0.83
$\eta = 1000, \quad r_0 = 0.25, \quad (x_c,\ y_c) = (-0.05,\ -0.05), n_x = 0.1, n_y = 0.1$						
$\mathcal{E}_{l,m}$	1.40e-03	1.48e-04	6.78e-05	1.59e-05	7.47e-06	4.21e-07
x_l, y_m	0.81,0.81	0.87,0.87	0.88,0.88	0.92,0.92	0.93,0.93	0.96,0.96

TABLE 5. Comparison of error and convergence rate with $\epsilon = 0.02$.

L	$\|\|\epsilon\|\|_2$	Θ_2	$\|\|\epsilon\|\|_\infty$	Θ_∞	c	$\|\|\epsilon\|\|_2$	Θ_2	$\|\|\epsilon\|\|_\infty$	Θ_∞
	$n_x = n_y = 1.0, c = 0.001$				$n_x = 0.9,\ n_y = 1$				
4	6.73e-1	—	2.37e-0	—	2.50	3.26e-1	—	7.06e-1	—
8	7.02e-2	3.3	3.48e-1	3.6	2.09	1.88e-2	4.1	4.84e-2	3.6
16	5.44e-3	3.7	2.58e-2	4.1	1.92	9.95e-4	4.2	5.11e-3	3.8
32	3.74e-4	3.9	1.93e-3	3.9	1.90	6.64e-5	4.0	3.32e-4	3.9

TABLE 6. Maximum-absolute errors and convergence order on a uniform grids.

L	$\|\|\epsilon\|\|_\infty$	Θ_∞	$\|\|\epsilon\|\|_\infty$	Θ_∞	$\|\|\epsilon\|\|_\infty$	Θ_∞
	$\epsilon = 1$		$\epsilon = 0.1$		$\epsilon = 0.01$	
2	8.87e-02	—	4.34e-01	—	6.01e-01	—
4	9.97e-03	3.3	1.60e-01	1.4	7.17e-01	0.3
6	7.23e-04	3.8	3.07e-02	2.4	6.38e-01	0.2
8	5.18e-05	3.8	3.13e-03	3.3	3.99e-01	0.7

8. Discussion and conclusions

The MQ-RBFs combined with high-order compact discretization significantly affect the solution values and convergence order. The scattered grid populates more grid points in the location of parallel, and boundary layers, infinitely smooth MQ-RBFs take care of the loss of smoothness inherited due to the discretization procedure, and compact characters preserve the convergence order with an optimized time-memory trade-off. The joint effect of MQ-RBF's shape parameter and grid stretching parameters can be tuned according to oscillations or layers that appear due to perturbation parameter changes. The proposed scattered grid network permits us to estimate a convergent and

TABLE 7. Maximum absolute errors and order of convergence using scattered grids.

L	n_x	n_y	$\|\|\epsilon\|\|_\infty$	Θ_∞	n_x	n_y	$\|\|\epsilon\|\|_\infty$	Θ_∞
2	1.00	1.0	4.34e-1	—	0.05	1.0	8.59e-1	—
4	0.50	1.0	7.91e-2	2.5	0.05	0.2	8.44e-2	3.3
8	0.50	1.0	7.18e-3	3.5	0.04	1.0	6.17e-3	3.8
16	0.58	1.0	6.81e-4	3.4	0.03	1.0	2.92e-4	4.4

TABLE 8. Comparison of solution error and convergence order at $\epsilon = 10^{-3}$.

L	c	n_x	n_y	$\|\|\epsilon\|\|_\infty$	$\|\|\Theta\|\|_\infty$	$\|\|\epsilon\|\|_\infty$ (Mohanty et al.[18])	$\|\|\Theta\|\|_\infty$
16	0.01	1.50	1.0	3.95e-04	—	6.71e-04	—
32	0.90	1.30	1.0	2.70e-05	3.9	8.80e-05	3.3
64	0.98	1.29	1.0	3.04e-06	3.1	5.69e-06	3.6

TABLE 9. Accuracies of solution error and convergence order.

L	$\|\|\epsilon\|\|_\infty$	Θ_∞	$\|\|\epsilon\|\|_2$	Θ_2	$\|\|\epsilon\|\|_\infty$	Θ_∞	$\|\|\epsilon\|\|_2$	Θ_2
Case-1	$\epsilon = 1,\ \sigma = 6.793248$				$\epsilon = \sigma = 10^{-5}$			
4	5.16e-07	—	3.46e-07	—	4.67e-02	—	2.97e-02	—
8	5.20e-08	3.3	3.05e-08	3.5	4.56e-03	3.4	2.60e-03	3.5
16	4.12e-09	3.7	2.28e-09	3.7	3.63e-04	3.7	1.94e-04	3.7
Case-2								
4	9.16e-07	—	6.03e-07	—	6.23e-01	—	4.09e-01	—
8	9.27e-08	3.3	5.23e-08	3.5	6.30e-02	3.3	3.55e-02	3.3
16	7.09e-09	3.7	3.76e-09	3.8	4.98e-03	3.7	2.64e-03	3.9

Appendix 1: Values of weight coefficients along x-directions.

$\alpha_l^{(0)}$	$(p_l - 1)(\sqrt{\alpha\beta} + \sqrt{\gamma})/[2h_{l+1}\sqrt{\alpha\beta}]$	$\alpha_l^{(2)}$	$(p_l + 1)(\sqrt{\alpha\beta} + \sqrt{\gamma})/[2h_{l+1}\sqrt{\gamma\alpha}]$
$\alpha_{l+1}^{(0)}$	$(\sqrt{\beta\gamma} + \sqrt{\alpha})/[2(1 + p_l)h_{l+1}\sqrt{\alpha\beta}]$	$\alpha_{l+1}^{(2)}$	$-(\sqrt{\alpha} + \sqrt{\beta\gamma})/[2(1 + p_l)h_{l+1}\sqrt{\gamma\alpha}]$
$\alpha_{l-1}^{(0)}$	$-p_l(\sqrt{\alpha\gamma} + \sqrt{\beta})/[2(1 + p_l)h_l\sqrt{\alpha\beta}]$	$\alpha_{l-1}^{(2)}$	$-(p_l + 2)(\sqrt{\alpha\gamma} + \sqrt{\beta})/[2h_l(p_l + 1)\sqrt{\gamma\alpha}]$
$\alpha_l^{(1)}$	$-(p_l + 1)(\sqrt{\alpha\beta} + \sqrt{\gamma})/[2h_{l+1}\sqrt{\beta\gamma}]$	$\alpha_l^{(3)}$	$-(\gamma_0\sqrt{\alpha\beta} + \beta_0\sqrt{\gamma})/[2(\alpha\beta)^{3/2}p_l h_l^2]$
$\alpha_{l+1}^{(1)}$	$(2p_l + 1)(\sqrt{\beta\gamma} + \sqrt{\alpha})/[2h_{l+1}(p_l + 1)\sqrt{\beta\gamma}]$	$\alpha_{l+1}^{(3)}$	$(\beta_1\sqrt{\gamma\beta} + \gamma_1\sqrt{\alpha})/[2(\alpha\beta)^{3/2}h_l^2 p_l(1 + p_l)]$
$\alpha_{l-1}^{(1)}$	$p_l(\sqrt{\alpha\gamma} + \sqrt{\beta})/[2(1 + p_l)h_l\sqrt{\beta\gamma}]$	$\alpha_{l-1}^{(3)}$	$(\beta_2\sqrt{\alpha\gamma} + \gamma_2\sqrt{\beta})/[2(\alpha\beta)^{3/2}h_l^2(p_l + 1)]$

accurate solution reconstruction of singularly perturbed elliptic PDEs in two dimensions. The MQ-RBFs combined compact architecture considers the solution approximations without consuming enough computational time and memory space (only a few nodes are needed). This happens due to the minimum grid stencils and specially designed iteration matrices in the computational loop. The extension to the proposed scheme for mildly nonlinear elliptic, parabolic, and hyperbolic PDEs in three dimensions with nonlinear gradients will attract numerical analysts.

ACKNOWLEDGMENT

S. Verma acknowledges South Asian University, New Delhi for providing research facilities and the Council of Scientific & Industrial Research Grant-in-aid (No.09/1112(0009)/2020-EMR-I) in the form of research fellowship.

Appendix 2: Values of weight coefficients along y-directions

$\beta_m^{(0)}$	$(q_m-1)\left(\sqrt{\sigma\rho}+\sqrt{\tau}\right)/\left[2k_{m+1}\sqrt{\rho\sigma}\right]$	$\beta_m^{(2)}$	$-q_m\left(\sqrt{\tau\rho}+\sqrt{\sigma}\right)/\left[2k_m\left(q_m+1\right)\sqrt{\rho\sigma}\right]$
$\beta_{m+1}^{(0)}$	$-\left(q_m+1\right)\left(\sqrt{\rho\sigma}+\sqrt{\tau}\right)/\left[2k_{m+1}\sqrt{\tau\sigma}\right]$	$\beta_{m+1}^{(2)}$	$q_m\left(\sqrt{\tau\rho}+\sqrt{\sigma}\right)/\left[2k_m\left(q_m+1\right)\sqrt{\sigma\tau}\right]$
$\beta_{m-1}^{(0)}$	$\left(q_m+1\right)\left(\sqrt{\rho\sigma}+\sqrt{\tau}\right)/\left[2k_{m+1}\sqrt{\rho\tau}\right]$	$\beta_{m-1}^{(2)}$	$-\left(q_m+2\right)\left(\sqrt{\tau\rho}+\sqrt{\sigma}\right)/\left[2k_m\left(q_m+1\right)\sqrt{\rho\tau}\right]$
$\beta_m^{(1)}$	$\left(\sqrt{\tau\sigma}+\sqrt{\rho}\right)/\left[2k_{m+1}\left(q_m+1\right)\sqrt{\rho\sigma}\right]$	$\beta_m^{(3)}$	$-\left(\tau_0\sqrt{\rho\sigma}+\sigma_0\sqrt{\tau}\right)/\left[2\left(\rho\sigma\right)^{3/2}q_mk_m^2\right]$
$\beta_{m+1}^{(1)}$	$\left(2q_m+1\right)\left(\sqrt{\tau\sigma}+\sqrt{\rho}\right)/\left[2k_{m+1}\left(q_m+1\right)\sqrt{\tau\sigma}\right]$	$\beta_{m+1}^{(3)}$	$\left(\tau_1\sqrt{\tau\sigma}+\sigma_1\sqrt{\rho}\right)/\left[2\left(\sigma\rho\right)^{3/2}q_mk_m^2\left(1+q_m\right)\right]$
$\beta_{m-1}^{(1)}$	$-\left(\sqrt{\tau\sigma}+\sqrt{\rho}\right)/\left[2k_m\left(1+q_m\right)\sqrt{\tau\rho}\right]$	$\beta_{m-1}^{(3)}$	$\left(\tau_2\sqrt{\rho\tau}+\sigma_2\sqrt{\sigma}\right)/\left[2\left(\rho\sigma\right)^{3/2}k_m^2\left(q_m+1\right)\right]$

Appendix 3: Values of parameter in Appendix-1 and Appendix-2

$\alpha=c^2h_l^2+1,\ \beta=c^2h_l^2p_l^2+1,\ \gamma=1+c^2\left(p_l+1\right)^2h_l^2,$
$\rho=c^2k_m^2+1,\ \sigma=c^2k_m^2q_m^2+1,\ \tau=1+c^2\left(q_m+1\right)^2k_m^2,$
$\beta_0=c^2h_l^2\{c^2h_l^2p_l\left(c^2h_l^2p_l^2+2p_l^2+2\right)+p_l^2+3p_l+1\}+2,$
$\beta_1=c^2h_l^2\left(c^2h_l^2p_l+p_l^2+p_l+1\right)+2,\quad \beta_2=p_l^3c^4h_l^4+2+c^2\left(p_l^2+p_l+1\right)h_l^2$
$\gamma_0=\left(2+c^2\left(p_l^2+p_l+1\right)h_l^2\right)\left(c^2h_l^2p_l+1\right)$
$\gamma_1=2+c^2h_l^2\{p_l^3c^4\left(p_l+1\right)h_l^4+p_lc^2\left(p_l^3+2p_l^2+2p_l+2\right)h_l^2+3p_l^2+3p_l+1\}$
$\gamma_2=2+c^2h_l^2\{c^2h_l^2\left(c^2h_l^2p_l^2\left(p_l+1\right)+2p_l^3+2p_l^2+2p_l+1\right)+p_l^2+3p_l+3\}$
$\tau_0=\left(2+c^2\left(q_m^2+q_m+1\right)k_m^2\right)\left(c^2k_m^2q_m+1\right)$
$\tau_1=c^2k_m^2\left(c^2k_m^2q_m+q_m^2+q_m+1\right)+2,\quad \tau_2=c^2k_m^2\left(c^2k_m^2q_m^3+q_m^2+q_m+1\right)+2$
$\sigma_0=c^2k_m^2\left(q_m^3c^4k_m^4+2c^2q_m\left(1+q_m^2\right)+q_m^2+3q_m+1\right)+2$
$\sigma_1=2+c^2k_m^2\left(q_m^2c^4\left(q_m+1\right)k_m^4+\left(2q_m^3+2q_m^2+2q_m+1\right)k_m^2c^2+3q_m^2+3q_m+1\right)$
$\sigma_2=2+c^2k_m^2\left(q_m^2c^4\left(q_m+1\right)k_m^4+\left(2q_m^3+2q_m^2+2q_m+1\right)k_m^2c^2+q_m^2+3q_m+3\right)$

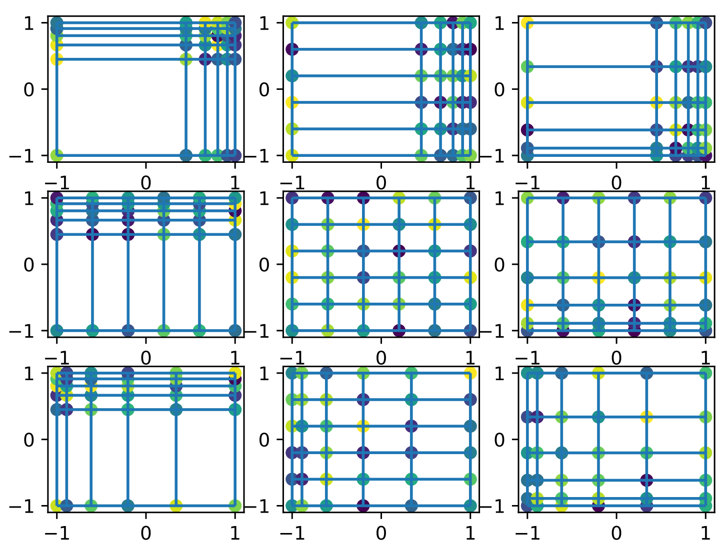

(g) $n_x>1, n_y<1$ (h) $n_x>1, n_y=1$ (i) $n_x>1, n_y>1$

FIGURE 1. Grid concentration for different values of n_x and n_y

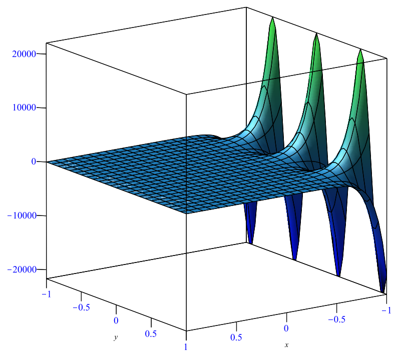

FIGURE 2. Surface plot at $P_e = 0.1$

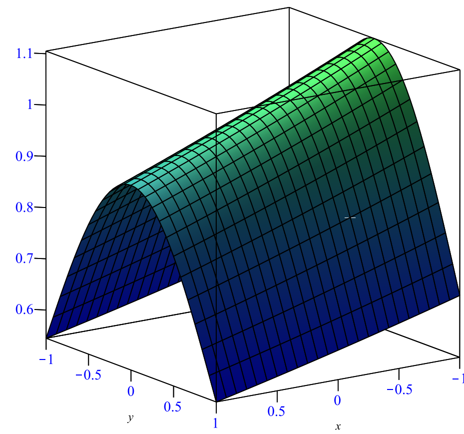

FIGURE 3. Surface plot at $P_e = 10$

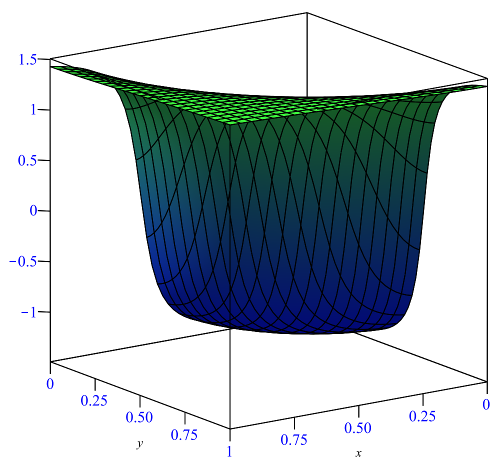

FIGURE 4. Surface plot at $\eta = 20,\ r_0 = 0.70$

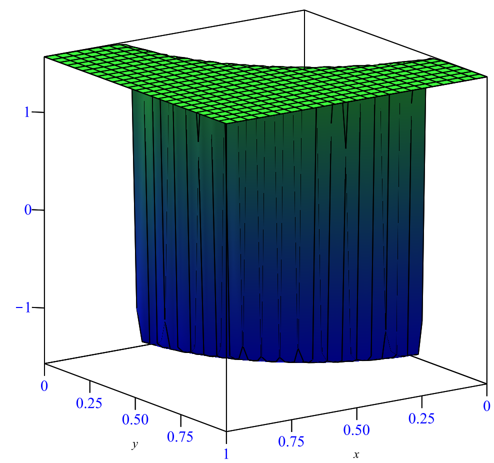

FIGURE 5. Surface plot at $\eta = 1000,\ r_0 = 0.70$

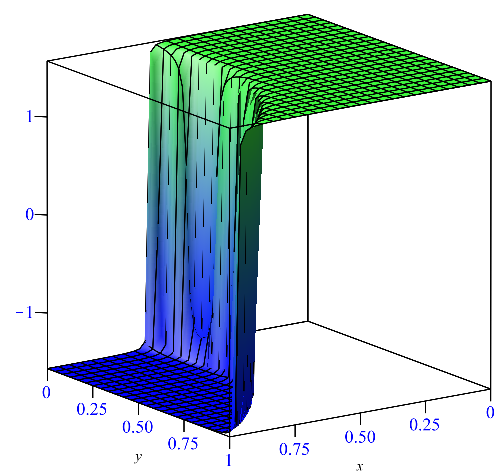

FIGURE 6. Surface plot at $\eta = 1000,\ r_0 = 0.92$

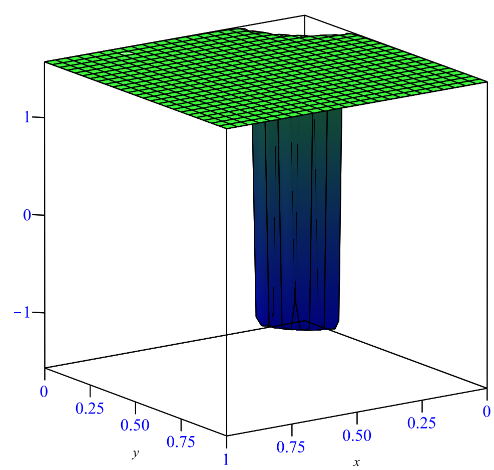

FIGURE 7. Surface plot at $\eta = 1000,\ r_0 = 0.25$

References

[1] V. Bayona, M. Moscoso, M. Carretero, and M. Kindelan, *RBF-FD formulas and convergence properties*, J. Comput. Phys., *229* (2010), 8281–8295.

[2] S. Banei and K. Shanazari, *On the convergence analysis and stability of the RBF-adaptive method for the forward-backward heat problem in 2D*, Appl. Numer. Math., *159* (2021), 297—310.

[3] D. Britz, *Digital simulation in electrochemistry*, Springer, Berlin, 2005.

[4] R. Feng and J. Duan, *High accurate finite differences based on RBF interpolation and its application in solving differential equations*, J. Sci. Comput., *76* (2018), 1785–1812.

[5] A. I. Fedoseyev, M. J. Friedman, and E. J. Kansa, *Continuation for nonlinear elliptic partial differential equations discretized by the multiquadric method*, Int. J. Bifurc. Chaos, *10*(2) (2000), 481–492.

[6] J.H. Ferziger and M. Peric, *Computational methods for fluid dynamics*, Springer, Berlin, 2002.

[7] P. Henrici, *Discrete variable methods in ordinary differential equations*, John Wiley and Sons, New York, 1962.

[8] N. J. Higham, *Accuracy and stability of numerical algorithms*, SIAM, Philadelphia, 2002.

[9] L. Jianyu, L. Siwei, Q. Yingjian, and H. Yaping, *Numerical solution of elliptic partial differential equation using radial basis function neural networks*, Neural Networks, *16* (2003), 729—734.

[10] N. Jha and N. Kumar, *A fourth-order accurate quasi-variable meshes compact finite-difference scheme for two-space dimensions convection-diffusion problems*, Adv. Differ. Equ., *64* (2017), 1–13.

[11] N. Jha and L. K. Bieniasz, *A fifth (six) order accurate, three-point compact finite difference scheme for the numerical solution of sixth order boundary value problems on geometric meshes*, J. Sci. Comput., *64* (2015), 898–913.

[12] N. Jha and B. Singh, *Fourth-order compact scheme based on quasi-variable mesh for three-dimensional mildly nonlinear stationary convection-diffusion equations*, Numer. Methods Partial Differ. Equ. (2020), 1–27.

[13] N. Jha and N. Kumar, *An exponential expanding meshes sequence and finite difference method adopted for two-dimensional elliptic equations*, Int. J. Model. Simul. Sci., *7*(2) (2016), 1–17.

[14] A. Komech and E. Kopylova, *Stationary Schrödinger equation, in Dispersion Decay and Scattering Theory*, John Wiley and Sons, 2012.

[15] H. Liu, B. Xing, Z. Wang, and L. Li, *Legendre neural network method for several classes of singularly perturbed differential equations based on mapping and piecewise optimization technology*, Neural Process. Lett., *51* (2020), 2891–913.

[16] M. Malekzadeh, S. Hamzehei-Javaran, and S. Shojaee, *Improvement of numerical manifold method using nine-node quadrilateral and ten-node triangular elements along with complex Fourier RBFs in modeling free and forced vibrations*, J. Appl. Comput. Mech., *7*(4) (2021), 2049–2063.

[17] W. F. Mitchell, *A collection of 2D elliptic problems for testing adaptive grid refinement algorithms*, Appl. Math. Comput., *220* (2013), 350–364.

[18] R. K. Mohanty, G. Manchanda, and A. Khan, *Operator compact exponential approximation for the solution of the system of 2D second order quasilinear elliptic partial differential equations*, Adv. Differ. Equ., *47* (2019), 1–36.

[19] A. Mohebbi and M. Saffarian, *Implicit RBF meshless method for the solution of two-dimensional variable order fractional cable equation*, J. Appl. Comput. Mech., *6*(2) (2020), 235–247.

[20] A. Mohsen, *A simple solution of the Bratu problem*, Comput. Math. Appl., *67* (2014), 26–33.

[21] A. D. Polyanin, *Handbook of linear partial differential equations for engineers and scientists*, Chapman and Hall/CRC, Boca Raton, 2001.

[22] G. Söderlind, I. Fekete, and I. Faragó, *On the zero-stability of multistep methods on smooth nonuniform grids*, BIT Numer. Math., *58* (2018), 1125–1143.

[23] G. I. Shishkin, and L. P. Shishkina, *Difference methods for singular perturbation problems*, CRC Press, 2010.

[24] M. Stynes, *Steady-state convection-diffusion problems*, Acta Numer., *14* (2005), 445–508.

[25] J. W. Thomas, *Numerical partial differential equations: conservation laws and elliptic equations*, Springer, New York, 1999.

[26] C. M. T. Tien, N. Mai-Duy, C. D. Tran, and T. T. Cong, *A numerical study of compact approximations based on flat integrated radial basis functions for second-order differential equations*, Comput. Math. Appl., *72* (2016),

2364–2387.
[27] R. S. Varga, *Matrix Iterative Analysis*, Springer, Berlin, 2000.
[28] G. B. Wright and B. Fornberg, *Scattered node compact finite difference-type formulas generated from radial basis functions*, J. Comput. Phys., *212* (2006), 99–123.
[29] D. M. Young, *Iterative solution of large linear systems*, Academic Press, New York, 1971.